

1 Grain-Size Analysis of the Late Pleistocene Sediments in the
2 Corinth Rift: Insights into Strait Influenced Hydrodynamics and
3 Provenance of an Active Rift Basin

4 Wenjun Kang¹, Shunli Li^{1*}, Robert L. Gawthorpe², Mary Ford³, Richard E. Ll. Collier⁴,
5 Xinghe Yu¹, Liliane Janikian⁵, Casey W. Nixon², Romain Hemelsdael⁶, Spyros
6 Sergiou⁷, Jack Gillespie⁸, Sofia Pechlivanidou², Gino De Gelder⁹.

7 1. School of Energy Resources, China University of Geosciences, Beijing, China

8 2. Department of Earth Science, University of Bergen, Norway

9 3. Université de Lorraine, ENSG, INP, France

10 4. School of Earth and Environment, University of Leeds, United Kingdom

11 5. Universidade Federal de São Paulo, Rua Carvalho de Mendonça, Brazil

12 6. Géosciences Montpellier, Université de Montpellier, France

13 7. Department of Geology, University of Patras, Greece

14 8. Center for Tectonics, Resources, and Exploration (TRaX), Department of Earth Sciences, School
15 of Physical Sciences, University of Adelaide, Australia

16 9. Institut de Physique du Globe de Paris, Sorbonne Paris Cité Université Paris Diderot, France

17 Present addresses: No.29, Xueyuan Road, Haidian District, School of Energy Resources, China

18 University of Geosciences, Beijing, 100083, China

19 *Corresponding author (e-mail: lishunli@cugb.edu.cn)

20 Abstract

21 Grain-size analysis of the sediments in borehole M0079A, which is located in the Corinth Rift,

22 was used to explore hydrodynamic conditions and provenance in the Late Pleistocene Corinth Rift.

23 Grain-size populations that were sensitive to the sedimentary environments were characterized by

24 frequency distribution, particle size-standard deviation, and probability cumulative curves. Our

25 results indicate the grain-size population component in the range 0.15-0.25 μm may be used as a

26 sensitive proxy for hyperpycnal flows, which have commonly been triggered by river floods from

27 the southern margin of the rift since ca. 0.593-0.613 Ma. The high-density plumes derived from the

28 longer rivers of the southern rift that were prevalent before ca. 0.593-0.613 Ma. When sediment is

29 supplied as hemipelagic deposition, the proportion of the total grain-size population that is in the

30 0.3-0.5 μm range becomes an index for suspension fall-out deposits. The core shows coarser

31 sediments during the marine periods and this may be linked to the current circulation related to the

32 Isthmia Strait opening. The study thus illustrates how the establishment of interbasinal straits can

33 influence the details of sedimentary hydrodynamics in the deep-water axis of an adjacent depocenter.

34 **Keywords:** sensitivity population; strait opening/closure; event deposits; hemipelagic;

35 hyperpycnal flows; sedimentary environments;

36

37 Grain-size analysis provides information about transportation history, source and depositional

38 conditions (Folk and Ward, 1957; Bui et al., 1990; Singh et al., 2007; Mir and Jeelani, 2015; Allen

39 et al., 2016; Singh et al., 2020). Early contributions are largely the grade of grain-size by Udden

40 (1898, 1914), Grabau (1904) and Wentworth (1922). Then, Trask (Woodford, 1933) and others

41 (Krumbein and Pettijohn, 1938; Otto, 1939) applied various statistical coefficients to characterize

42 the size-frequency distribution of clastic sediments (Sahu, 1964). In the 1950s and 1960s, grain-size

43 analysis was widely used in the identification of hydrodynamic conditions and as the basis for facies

44 analysis (Passega, 1957; Mason and Folk, 1958; Fuller, 1961; Sahu, 1964; Friedman, 1967; Visher,
45 1969). Grain-size analysis has come a long way in sedimentology, including here the McLaren (1985)
46 method to predict sedimentary paths (transport directions). Since the 1990s, despite the
47 representation and application of methods of grain-size analysis, data in geology have remained at
48 the level of several decades ago, whilst some scholars still put forward new grain-size indexes and
49 methods, such as particle size ratio (Ding et al., 1991), sensitive components (Xiao et al., 2006),
50 fractal dimension (Tyler and Wheatcraft, 1992), particle size trend analysis (Gao and Collins, 1994)
51 and so on, to restore transportation history, depositional conditions, provenances and transport
52 dynamics, paleoenvironment and paleoclimate (Yuan et al., 2011; Lu et al, 2013; Mir and Jeelani,
53 2015; Kanhaiya et al., 2016; Gamboa et al., 2017; Zhang et al., 2021). The method of using sediment
54 grain-size populations to analyze the changes in sedimentary environments has been well applied in
55 the study of oceanic shelf and continental sediments all over the world (Prins et al., 2000; Xiao et
56 al., 2006; Mir and Jeelani, 2015; Singh et al., 2020), including the fine-grained fractions (silt and
57 clay) of proximal strait-adjacent deposits indicate tide processes (Beelen et al., 2022), the grain-size
58 distribution of Quaternary deep-sea sediment in the Sumba Strait is influential on organic material
59 (Zulhikmah et al., 2020).

60 Grain-size plays a fundamental role in determining the spatiotemporal scales over which
61 internal dynamics of sedimentary systems operate (Ganti, Lamb, & McElroy, 2014; Watkins et al.,
62 2020). The accumulation of deposits under straits-controlled current amplification (Cavazza and
63 Longhitano, 2022; Rossi et al., 2022) also contains grain-size information that reflects the dynamics
64 of sedimentary systems. Moreover, McNeill et al. (2019) suggest that at the glacial-interglacial

65 timescale (100's ka) climatic and environmental change strongly affects the nature and volume of
66 sediment within the Corinth Basin (sediment fluxes, grain-size, lithostratigraphy, etc.), and infer
67 that: "These orbital-timescale changes in rate and type of basin infill will likely influence early rift
68 sedimentary and faulting processes, potentially including syn-rift stratigraphy, sediment burial rates,
69 and organic carbon flux and preservation on deep continental margins worldwide."

70 According to the onshore sedimentary records and offshore seismic stratigraphy, major
71 evolution phases of the paleoenvironments in the Corinth Rift were recognized by geologists in
72 recent years (Sachpazi et al., 2003; Ford et al., 2007; Nixon et al., 2016). The changing
73 environmental conditions reflected by the microfossil assemblages were interpreted to arise from
74 fluctuating eustatic sea levels with respect to the bounding sills (or straits) of the Gulf of Corinth
75 (Bell et al., 2009; Taylor et al., 2011; Gawthorpe et al., 2018; McNeill et al., 2019). The cores
76 recovered by IODP Expedition 381 also provide the first evidence of sea-level driven changes in
77 paleoenvironments of an active deep-water rift basin over hundreds of thousands of years (0-750ka)
78 (Shillington, D.J. et al., 2018). Recently, Gawthorpe et al. (2022) suggest that the height of rift
79 segment boundaries of the Corinth Rift control the influx of marine waters from the global ocean,
80 and discuss how the change of marine bioturbated, non-marine bedded and laminated packages are
81 linked to the opening or closure of the basin to the open ocean. Further confirmation of the
82 sedimentary processes/hydrodynamic changes in response to the open strait vs closed/non-strait
83 state of the basin have been described previously (Collier et al., 2000; Scholz et al., 2007; Li et al.,
84 2018). However, detailed discussions of what impact fluctuations between highstand marine
85 conditions and lowstand isolated/semi-isolated conditions will have on the grain-size of sediment

86 or what kind of grain-size populations can reflect the hydrodynamics and provenance of sediments
87 in the Gulf of Corinth are rare (Pechlivanidou et al., 2018; Watkins et al., 2020; Gelder et al., 2021;
88 Maffione and Herrero-Bervera, 2022).

89 In this contribution, we present a study of the sediments of the Late Pleistocene in the
90 depocenter ~20 km downstream from the paleo-strait connecting the Corinth Rift, and attempt to
91 interpret differences in the sediment supply during the gulf when periodically sea-connected and
92 when an isolated lake with intermittent marine incursions, from the variability of sensitive
93 populations of grain size. This work is the results of extraction of grain-size populations sensitive
94 to the sedimentary environments based on the frequency distribution curve, the particle size –
95 standard deviation method, and the probability cumulative curve. We use these, together with the
96 discussion of the implied hydrodynamic conditions and provenance, in our aim to: (i) characterize
97 the grain-size populations of sediments under different flow processes/mechanisms; (ii) use
98 variability of sensitive grain-size populations to identify the main hydrodynamic conditions and
99 provenances within the Late Pleistocene active rift, and (iii) discuss the controls of close/open (non-
100 strait/strait) states on basin floor sedimentation and provenance evolution in the Corinth Rift. In
101 other active rift basins that were controlled by straits with interacting processes in varying marine
102 and non-marine environments (e.g., the Red Sea. Hussain et al., 2022), sedimentation and grain-size
103 characteristics of sediment show similarly complicated features. This study will provide insights
104 into the variability of hydrodynamics and provenance by analysis of sensitivity in grain-size
105 populations.

106 Geological settings

107 The Corinth active rift, geographically located in Greece in the north-eastern Mediterranean Sea
108 (Fig. 1a), is one of Europe's most seismically active areas, accompanied by rapid and local crustal
109 stretching. Current extensional rates reach 10-15 mm/yr (Clarke et al., 1998; Briole et al., 2000;
110 Bernard et al., 2006). Structurally, it is located between the North Anatolian Fault and the
111 Kefalonia Fault/Greek subduction zone (Ford et al., 2016; Gawthorpe et al., 2018) (Fig. 1a). The
112 Corinth Rift is also a ~100×30 km high-strain band in central Greece that experiences N-S extension
113 (Bell et al., 2009), showing the structural features of a dustpan-shaped faulted depression or
114 asymmetric graben (Fig. 1b).

115 Nowadays, the eastern end of the Gulf of Corinth is connected by the Corinth Isthmus
116 (currently a desolate highland with an altitude of 90 m (Fig. 1a) at the basin margins). The Corinth
117 Isthmus, however, was periodically connected with the Corinth basin during periods of high sea
118 level between 0.1-0.6 Ma (Gawthorpe et al., 2018). The western end of the Gulf of Corinth is
119 connected to the Mediterranean Sea across the Rion Sill (60-70 m below sea level) (Fig. 1a). This
120 sill is interpreted to have controlled the connection since at least 200 ka between the Ionian Sea and
121 the Gulf of Corinth (Perissoratis et al., 2000; Bell et al., 2008). More recent studies show that the
122 Rion Sill was filled by sediments of the Rodini fluvial system (see Gawthorpe et al., 2018, their
123 figure 13b) before 0.8 Ma, and the huge delta blocked the connection between the western part of
124 the Gulf of Corinth and the ocean. But the elimination of land barriers and the opening of a strait is
125 interpreted to have occurred since 0.6 Ma at the western end (Gawthorpe et al., 2018). Meanwhile,
126 due to the influence of glacial and interglacial periods, the fill of the Corinth Rift has experienced

127 continental, lacustrine and marine/lacustrine alternating phases in its evolution (Ford et al., 2013).

128 The earliest known syn-rift sediments (ca. 3.6-4 Ma) within the Corinth Rift outcrop onshore
129 (Collier and Dart, 1991; Collier and Thompson, 1991; Bell et al., 2009), while offshore basins
130 equivalent to the early syn-rift deposits exposed in northern Peloponnesos were either not deposited
131 or preserved as far north as the present rift, or they were thin and pinched out northwards at this
132 period (Nixon et al., 2016). Nixon and others (Nixon et al., 2016) proposed ages for seismic
133 stratigraphic Unit 1 (ca. 2-1.5 Ma to 0.6 Ma; see Fig. 1b) and Units 2 (ca. 0.6 Ma to present; see Fig.
134 1b) that correspond with age estimates for the onshore Middle Group and Upper Group (Rohais et
135 al., 2007; Leeder et al., 2012; Ford et al., 2013), respectively. Around 0.8 Ma, the overall migration
136 of fault activity in the basin was northward, but major faults bounding the Corinth Basin (largely
137 beneath the present-day Corinth Isthmus) were largely inactive in this period, creating local
138 depocenters and highs (Collier and Dart, 1991; Collier and Thompson, 1991; Gawthorpe et al.,
139 2018), and the main depocenter of the Corinth Gulf continues to deepen to the west of the Isthmus.
140 With the northward migration of the fault activity, N-dipping faults occupy a dominant position in
141 controlling the basin subsidence (except in the western basin) (Nixon et al., 2016). By this time, the
142 main rift depocenter has become narrower, forming the modern asymmetric graben or half-graben
143 (Fig. 1b) (Bell et al., 2008; Gawthorpe et al., 2018).

144 Site M0079A in the Gulf of Corinth, the focus of observations in this paper, is located between
145 the Corinth Isthmus ~30 km to the southeast and the Rion Sill ~80 km to the northwest (Fig. 1a).
146 The sediments recovered from site M0079A may be derived from southern fluvial systems, deltas,
147 turbidity currents and hemipelagic suspension (Bell et al., 2008; Ford et al., 2016; Gawthorpe et al.,

148 2018). Since 0.8 Ma, the water depth has seen a relative deepening trend (i.e., deepening events;
149 Ford et al., 2016), due to the fluctuation of sea level relative to the boundary of the basin (Perissoratis
150 et al., 2000), ongoing background hanging wall subsidence, and the apparently fortuitous elevation
151 of horst blocks at basin margins (Piper et al., 1988), and migration of faults (Collier and Dart, 1991;
152 Ford et al., 2016).

153 Materials and chronological framework

154 Data and methods

155 Sediments sampling and grain-size measurements

156 The research datasets come from the Corinth Active Rift Development IODP Expedition 381. This
157 study focuses on the sampling of the 249-323 mbsf and 540-630 mbsf intervals of hole M0079A, a
158 collection of 111 samples. Samples were extracted from the M0079A cores at the spacing of 0.5 to
159 2 m, and the length of a single sample is 2 cm.

160 The grain-size measurements were carried out on the Mastersizer 2000, which is made by
161 Malvern Company of the United Kingdom. It measures in the range of 0.02-2000 μm and can
162 provide the volume percentage content of each particle size component. The grading standard
163 followed the Udden-Wentworth grade scale (Udden, 1914; Wentworth, 1922). Grain-sizes were
164 represented by the ϕ value (Krumbein, 1934). Grain-size parameters (i.e., particle size, standard
165 deviation and skewness; later in this article) were calculated using the formulas of McManus (1988).
166 The detailed pre-processing of the grain-size analysis sample was as follows: (1) 10% H_2O_2 was
167 added to remove organic matter and soluble salt (NaCl, KCl et al., in seawater) from the sediment;
168 (2) 10% HCl, was added to remove carbonate cements, then distilled water is added and left for
169 more than 12 hours; (3) 10% sodium hexametaphosphate was added and fully dispersed in an

170 ultrasonic oscillator; (4) the treated sediment was put into a beaker containing distilled water, and
171 the sediment was pumped into the laser particle size analyzer through high-speed blades; (5) the
172 particle size data were obtained on the computer connected to the laser particle size analyzer.

173 Source of reference data

174 The X-ray fluorescence (XRF) measurements were carried out on the XRF-scanner in MA
175 RUM (University of Bremen) and the data of XRF are new in this paper. Preliminary met
176 hods and results of the XRF data of IODP Expedition 381 are accessible on [https://iodp.pangaea.de/front_content.php?idcat=616&count=10&q=citation%3A%22X-Ray%20fluorescence%20\(XRF\)%20scanning%22](https://iodp.pangaea.de/front_content.php?idcat=616&count=10&q=citation%3A%22X-Ray%20fluorescence%20(XRF)%20scanning%22).

179 In order to better use data of the XRF, all the key element intensities were calibrated against
180 16 representative samples taken from the 249-323 mbsf and 540-630 mbsf intervals of hole M0079A.
181 The LRCE-based calibration undertaken for the study section involved additive log transformation
182 (alr) of intensity and concentration data following Weltje & Tjallingii (2008) and Hussain et al.
183 (2020). The original data on element intensity and concentration were obtained during IODP
184 Expedition 381. Regression analysis showed tight correlations between intensity and concentration
185 for the majority of elements as indicated by high R2 values (typically >0.98; see calibration in Fig.
186 2a). Based on the goodness-of-fit (highest R2 value with the maximum number of elements), Ca
187 was selected as an optimum denominator for the calibrated log ratio data (see inset data table in Fig.
188 2b, 2c, and 2d).

189 Calcareous nannofossils, non-marine diatoms and benthic foraminifera were counted from core
190 catcher samples offshore and examined at approximately 5-m intervals. Qualitative counts data of
191 calcareous nannofossils and non-marine diatoms were from McNeill et al. (2019), which were based

192 on the Cascading Count Method (Styzen, 1997), with specific counting criteria available in the paper
193 of McNeill et al. (2019).

194 Grain-size populations

195 To separate a single grain-size population from all frequency distribution curves, this paper
196 uses the standard deviation-particle size method (Sun et al., 2002; Xiao et al., 2006), which is more
197 sensitive to fine populations, and obtains the number and distribution range of sensitive grain-size
198 populations. For each 100 particle size classes given by the Mastersizer 2000, the standard deviation
199 of 111 samples was calculated, and the relationship between standard deviation and particle size is
200 outlined in the section on sensitivity populations.

201 In this paper, the probability accumulation curve was used for the first time for extracting the
202 grain-size populations sensitive to environmental changes. The probability accumulation curve was
203 drawn with reference to the standard probability curve plate of Visher (1969), in which the extended
204 abscissa 4.5-8.5 ϕ segment was added to better reflect the grain-size characteristics of sediments in
205 the study area.

206 Age model

207 The boundary age of the M0079A subunit in this study was obtained by Maffione and Herrero-
208 Bervera (2022), using magnetostratigraphic and relative paleointensity (RPI) constraints from 885
209 discrete samples from International Ocean Discovery Program (IODP) Hole M0079A to generate
210 an unprecedented high-resolution (~15 kyr) age model for the youngest part of the Corinth's
211 offshore syn-rift sequence.

212 Description of the drilled cores

213 Intervals of 265.84-269.31 mbsf, 270.885-275.435 mbsf, 298.14-307.92 mbsf and 540-544 mbsf
214 were interpreted as marine deposits, while intervals of 249-265.84 mbsf, 269.31-270.885 mbsf,
215 275.435-298 mbsf, 307.92-323 mbsf and 544-558.29 mbsf were attributed to isolated/semi-isolated
216 lake deposits. The interval of 558.29-630 mbsf was interpreted as intermittent marine incursion
217 deposits.

218 Isolated/semi-isolated sedimentary environments

219 The bulk of the deposition within the isolated/semi-isolated sediment succession was composed of
220 light grayish-green mud shale and gray-white calcareous argillaceous siltstone. The latter were
221 intercalated in the transition zone between non-marine (i.e., isolated/semi-isolated) and marine
222 formations (Fig. 3 and Fig. 4), indicating episodic confinement within a lacustrine system (Moretti
223 et al., 2004). Gray-white calcareous argillaceous siltstone was interpreted as chemical deposition of
224 aragonite in an oversaturated environment (Moretti et al., 2004; Lykousis et al., 2007). Non-marine
225 diatoms that reflect the isolated/semi-isolated conditions (McNeill et al., 2019) occurred in intervals
226 of 249-265.84 mbsf, 269.31-270.885 mbsf, 275.435-298 mbsf, 307.92-323 mbsf and 544-558.29
227 mbsf, where trace fossils such as *Teichichnus* and *Phycosiphon* appear at the same time. *Teichichnus*
228 (Fig. 5) commonly are found in lower shoreface to offshore environments associated with the
229 Cruziana ichnofacies (Pemberton et al., 2009). *Phycosiphon* (Fig. 5) reflects isolated basins or semi-
230 enclosed lagoons and bays (Jiang, 2010).

231 Among the geochemical indices, the enrichment of Sr is often related to the aragonite needles
232 occurring more frequently within the (semi-)isolated interval than in the marine interval, especially

233 in the transition from marine to (semi-)isolated environments (McNeill et al., 2019; Gelder et al.,
234 2021). Sr was enriched at 265 mbsf, 269 mbsf, 271 mbsf, 276 mbsf, 298 mbsf, 307 mbsf, 542 mbsf,
235 544 mbsf and 588-592 mbsf, and most of the sediments were gray-white calcareous argillaceous
236 siltstone (Fig. 3 and Fig. 4). The gray-white calcareous argillaceous siltstone was interpreted as
237 chemical precipitation in the water column of an evaporitic lake (Moretti et al., 2004). The Mg
238 partition coefficient in calcite decreases with increasing salinity, and the partition coefficient of Sr
239 in aragonite is unaffected by salinity variations ((Zhong and Mucci, 1989). The enrichment of Sr,
240 thus, is an indicator of the end and early stage of marine or isolated/semi-isolated conditions.

241 Ca and the Ca/Sr ratio show a consistent trend, presenting high values in the 249-265.84 mbsf,
242 269.31-270.885 mbsf, 275.435-298 mbsf, 307.92-323 mbsf and 544-558.29 mbsf intervals (Fig. 3
243 and Fig. 4; indicated by the black solid arrow), whereas Mn and Br show low values in the same
244 intervals. Freshwater influx during the transitional stages of semi-isolated conditions induced
245 salinity decrease of the water. Incorporating riverine Sr influx, precipitation rates of aragonite would
246 increase significantly when salinity decreased (Zhong and Mucci, 1989; Bickle et al., 2005).
247 Subsequently, decreasing atmospheric CO₂ and an increase of carbonate erosion onshore (Nizou et
248 al., 2010; Shillington et al., 2019, McNeill et al., 2019) during glacial periods drove supersaturation
249 of dissolved CO₃²⁻ and Ca²⁺ in the Corinth Rift, which resulted in the enrichment of Ca in the 249-
250 265.84 mbsf, 269.31-270.885 mbsf, 275.435-298 mbsf, 307.92-323 mbsf and 544-558.29 mbsf
251 intervals (Fig. 3 and Fig. 4; indicated by the black solid arrow).

252 Marine sedimentary environment

253 The marine succession mostly consists of purplish-green siltstone with bioturbation. Between

254 265.84-269.31 mbsf, 270.885-275.435 mbsf, 298.14-307.92 mbsf and 540-544 mbsf, numerous
255 calcareous nannofossils and benthic foraminifera (Fig. 3 and Fig. 4) indicated a fully marine
256 environment (Heezen et al., 1966; McNeill et al., 2019), with some trace fossils (i.e., *Phoebichnus*,
257 Fig. 5). *Phoebichnus* is a large, radiating trace fossil most commonly found in shallow marine
258 siliciclastic deposits (Evans, 2016).

259 Mn shows high-values in the 265.84-269.31 mbsf, 270.885-275.435 mbsf, 298.14-307.92 mbsf
260 and 540-544 mbsf intervals, and the value of Br in the middle of these intervals is higher than on
261 either side (Fig. 3 and Fig. 4; indicated by the black dashed arrow). The dissolved Mn is interpreted
262 to have been oxidized into MnO₂ by adequate oxygen and subsequently sedimented to the sea floor
263 (Mangini et al., 1990, Shillington et al., 2019) in interglacial periods, inducing higher values of Mn
264 in the 265.84-269.31 mbsf, 270.885-275.435 mbsf, 298.14-307.92 mbsf and 540-544 mbsf intervals.
265 Br-containing organic compounds are mainly formed by macro- and microalgae (Quack and Wallace,
266 2003). The high salinity and low temperatures could increase the production of micro-organisms
267 (Abrahamsson et al., 2018), and contribute to forming the high concentrations of Br. The enrichment
268 and concentration increase of Br indicates marine conditions and opening of the strait (Rion sill
269 or/and Corinth Isthmus) (Malcolm and Price, 1984; Jiang, 2010; Caley et al., 2011).

270 Intermittent marine incursions

271 In the 558.29-630 mbsf interval, the lithofacies were mainly composed of light grayish-green
272 mudstone, with alternations of purplish-green, grayish-white, gray-white calcareous argillaceous
273 siltstone, light-yellow siltstone and brownish-brown gravel sandstones (Fig. 4). The intermittent
274 occurrence of the trace fossil *Phoebichnus* (Fig. 5), in the intervals of 597-600 mbsf, 614-615 mbsf

275 and 626-627 mbsf was accompanied by sparse calcareous nannofossils (Fig. 4). The rarity of benthic
276 foraminifera in the interval 558.29-630 mbsf points to chronically reduced salinity (Kontopoulos
277 and Avramidis, 2003). Fe, Br, and the Mg/Ca ratio show a periodic fluctuation with a narrow range
278 in the 558.29-630 mbsf interval (Fig. 4; indicated by the red arrow). Br high-concentrations are
279 directly related to the marine conditions (Malcolm and Price, 1984). Trends of Br content were
280 opposite to that of terrigenous elements (Fe) and Mg/Ca ratio (a decline reflecting the decrease of
281 water temperature; a rise indicating interglacial periods and marine environments; Lea et al., 2000,
282 Shillington et al., 2019, McNeill et al., 2019) in the 558.29-630 mbsf interval.

283 Furthermore, according to the characteristics of the sediment in the Aliki lagoon (Gulf of
284 Corinth) (Kontopoulos and Avramidis, 2003), we infer that the 558.29-630 mbsf interval was
285 dominated by an isolated lake, with only intermittent marine incursions.

286 Grain-size features

287 This paper extracts the grain-size populations which may be sensitive to hydrodynamics and
288 provenance under different environments (isolated/semi-isolated, marine and intermittent marine)
289 of the Corinth Rift by three methods of grain-size analysis. The results show that the grain-size
290 populations $<3.9 \mu\text{m}$ (clay), $0.15\text{-}0.25 \mu\text{m}$, $0.3\text{-}0.5 \mu\text{m}$, $<62.5 \mu\text{m}$ (clay and silt), $88.4\text{-}250.0 \mu\text{m}$
291 (very fine to fine sand) and $176.8\text{-}500.0 \mu\text{m}$ (fine to medium sand) were sensitive to the changes of
292 sedimentary environments and hydrodynamic conditions in the Gulf of the Corinth.

293 Frequency distribution curve

294 The frequency distribution curves of sediments were mostly of trimodal or four peaks in the research
295 interval of M0079A, and contain coarse and fine tails (Fig. 6b). The frequency distribution curves

296 of isolated/semi-isolated and marine environments cross each other, and are hard to distinguish, but
297 the content of components of $<3.9 \mu\text{m}$ is higher than that in marine environments (Fig. 6b). The
298 multimodal character frequency distribution curve generally indicates changes of multiple
299 provenance, transportation and dynamic conditions. From the skewness (S_k)-standard deviation (σ_ϕ)
300 diagram (Fig. 6a), the sampling points of isolated/semi-isolated are in the range of $-0.13 < S_k < 0.83$,
301 $2.49 < \sigma_\phi < 3.27$, the sampling points of marine are in the range of $-0.34 < S_k < 0.48$, $2.46 < \sigma_\phi < 3.54$,
302 the sampling points of intermittent marine are in the range of $-0.27 < S_k < 0.74$, $2.34 < \sigma_\phi < 3.78$, and
303 the sorting is poor, nearly symmetrical and positive. The sorting and skewness of sampling points
304 in marine and intermittent marine are similar, and nearly symmetrical, indicating that the sediment
305 was mixed with many components, and the coarse-grained and fine-grained components are
306 approximately equal. However, the sorting and skewness of sampling points are concentrated in
307 isolated/semi-isolated, and positive is dominant, indicating that the coarse-grained components are
308 dominant for sediment.

309 In addition, all the frequency distribution curves have a partially similar trend (Fig. 6b). This
310 trend was clay fraction ($<3.9 \mu\text{m}$), with two main peaks, which may reflect the influences of single
311 provenance and multi-hydrodynamic conditions on clay fraction (for example, the trend may
312 indicate a single provenance of a river, with high-density plume or hyperpycnal flows triggered by
313 floods, and other transportation). However, the curve trend ($>3.9 \mu\text{m}$) was random with respect to
314 the curve trend ($<3.9 \mu\text{m}$), which may indicate a more complex mix of sources and/or depositional
315 processes. Therefore, this section only selects the clay fraction ($<3.9 \mu\text{m}$) as an index for the
316 sensitivity population.

317 Sensitivity populations

318 Several peaks and troughs were observed in Fig. 7. In three curves of standard deviation vs. particle
319 size for core M0079A samples, the trimodal grain-size interval ranges with similar trends were 0.15-
320 0.25 μm , 0.6-0.9 μm and 3-5.5 μm , respectively (Fig. 7). They have higher standard deviations,
321 especially in the range of 0.15-0.25 μm (Fig. 7), which represents a population of grains with the
322 highest variability through time (Xiao et al., 2006). In contrast, two troughs, at 0.3-0.5 μm and 0.9-
323 1.5 μm particle size intervals (Fig. 7), have low standard deviations, which indicate that these ranges
324 of the grain-size population do not change importantly in all the samples of sediment. In the
325 sensitivity curves at particle sizes $> 0.5 \mu\text{m}$ (Fig. 7), there are no visible differences between the
326 peak and trough values. Therefore, grain-size populations of 0.15-0.25 μm and 0.3-0.5 μm were
327 selected with reference to the maximum and minimum value of standard deviations in this paper.

328 Probability cumulative curve

329 The coarse and fine cut-off points reflect the significant change of the material size distribution in
330 the two-section type (Fig. 8c) and three-section type (Fig. 8d) formula (Lin et al., 2005), and the
331 zero-section type (Fig. 8a) content ($< 62.5 \mu\text{m}$) was extracted into grain-size populations, these being
332 sensitive to environmental changes and, specifically, to transport process as outlined below.

333 The probability cumulative curve types of borehole M0079A were mainly divided into four
334 types: zero-section type (i.e., with particle size less than suspension populations), one-section type
335 (i.e., suspension populations), two-section type (i.e., saltation and suspension populations) and
336 three-section type (i.e., traction, saltation and suspension populations), showing little discrimination
337 for different environments in the study sections. The shape of the zero-section type probability

338 cumulative curve exceeds the standard probability cumulative curve chart (Fig. 8a), which shows
339 all of the sediments represent a suspended load population. Similarly, the one-section type
340 probability cumulative curve, like a straight line (Fig. 8b), indicates that almost all of them were
341 suspension populations. The proportion of the suspended load population is about 98% in the two-
342 section type and is about 90% in the three-section type. The results show that the probability
343 cumulative curve of all samples describes a mainly suspension population with a size of less than
344 62.5 μm .

345 The probability cumulative curve of the two-section type was also composed of a saltation
346 population and a suspension population (Fig. 8c). Compared with the two-section type curve, the
347 probability cumulative curve of the three-section type has more of a traction population (Fig. 8d).
348 Whether it is two-section or three-section type, the range of the fine cut-off point is roughly between
349 2.0-3.5 ϕ . This grain-size population represents the coarsest particles that can be suspended,
350 indicating the transition between transportation modalities (i.e., the size of a sediment particle that
351 maybe held in suspension is dependent upon turbulence), and reflects the change in the size
352 distribution of the wash load or material transported dominantly in suspension (Lane, 1938; Visher,
353 1969). In contrast, the range of the coarse cut-off point is between 1.0-2.5 ϕ in the three-section
354 type, which represents the coarsest particle that can jump. This transition has been attributed by
355 some workers as the junction between the Stokes and Impact Law formulae (Fuller, 1961; Visher,
356 1969), and this might be interpreted as the size where inertial forces cause rolling or sliding of
357 particles rather than saltation (Visher, 1969). However, saltation and traction populations are
358 difficult to transport beyond the shoreface region unless there are vigorous bottom currents (e.g.,

359 ocean-bottom currents, hyperpycnal flows, contour currents, etc.) or other trigger mechanisms (e.g.,
360 seismic, volcanic activity, tsunami wave, monsoon flooding, etc.).

361 Discussion

362 Interpretation of the grain-size populations

363 Centimeter-thick sand layers and homogeneous mud (e.g., Fig. 10, 79A-9) were observed in the
364 cores with variation in population content at $<3.9 \mu\text{m}$, $0.15\text{-}0.25 \mu\text{m}$, $0.3\text{-}0.5 \mu\text{m}$, $<62.5 \mu\text{m}$, 88.4-
365 $250.0 \mu\text{m}$ and $176.8\text{-}500.0 \mu\text{m}$ (e.g., at 259.9 mbsf, 540.67mbsf and 565.23 mbsf). Origins and
366 trigger mechanisms of these sedimentary events in the Gulf of Corinth may include seismically
367 induced gravitational mass flows (Nomikou et al., 2011; Sergiou et al., 2016), earthquake-triggered
368 tsunamis (Stefatos et al., 2006), gravitational collapse-initiated gravity flow in ancient deltas along
369 the southern margin (Backert et al., 2010; Gawthorpe et al., 2017; Fig. 9, a-1 and a-2), and density
370 flows in the modern submarine canyons (McNeill et al., 2005) of the Gulf of Corinth. These flows
371 might be enhanced by fluxes of sediment from the strait (Collier and Thompson, 1991), contributing
372 to the delivery of shallow sediments to the deep-water basin axis. Seismicity may be the primary
373 controlling factor of these sedimentary events (Gelder et al., 2021; Gawthorpe et al., 2022), taking
374 into account the Corinth Rift is one of Europe's most seismically active areas (McNeill et al. 2019)
375 and the characteristics of some sedimentary events have allowed the interpretation of earthquake-
376 induced deposits from cores in the central part of the Corinth Rift (Campos et al., 2013). In addition,
377 the probability accumulation curves of the samples of event deposits (i.e., 79A-9, 79A-56, 79A-73;
378 Fig. 10) are mainly three-section type types (Fig. 10), and the proportion of the total content of
379 saltation and traction populations is more than 20% (Fig. 10), which need vigorous slope parallel

380 bottom currents to transport. The main characteristics of the event deposits were as follows (Fig.
381 10): a peak in the 0.3-0.5 μm population component, a decrease of population content at 0.15-0.25
382 μm , a relatively significant increase of population content at the coarse and fine cut-off points, and
383 a visible decrease of the $<3.9 \mu\text{m}$ and $<62.5 \mu\text{m}$ population components.

384 Sedimentary structures representing wave actions were not observed in the cores (e.g., at
385 288.00 mbsf, 289.13 mbsf, 314.78 mbsf, 544.37 mbsf, 600.34 mbsf; Fig. 10) which suggests this
386 site (Fig. 1a) was located at a depth beyond the reach of sea or lake waves during this period. The
387 content of the grain-size population of 0.3-0.5 μm from the 249-323 mbsf section (Fig. 10) has only
388 one larger peak at 259.9 mbsf and was stable at about 0.8% in the rest of the section. According to
389 the known environmental background (see Fig. 3 and Fig. 4; Bell et al., 2009; Gawthorpe et al.,
390 2018), the results indicate that the change of the content of this population of 0.3-0.5 μm was almost
391 unaffected by the alternation of marine and isolated/semi-isolated (i.e., continental) environments.
392 Therefore, this content of the grain-size population from 0.3-0.5 μm was maintained at 0.8%, which
393 was likely to represent the suspended deposits under extremely low-energy, perhaps as an indicator
394 of hemipelagic deposit (provenance 1) as detailed in the next section.

395 The population content of 0.15-0.25 μm grains was zero (Fig. 10) in some sections (e.g.,
396 between 275 mbsf and 290 mbsf), with the probability accumulation curves of samples mainly one-
397 section type and zero-section type (Fig. 10), and the proportion of the finer-grained particles ($\phi > 3$)
398 was more than 99% (Fig. 10). The core was dominated by massive mudstone without recognizable
399 bedding near the sampling location (Fig. 10; see 79A-29, 79A-30, 79A-49, etc.). The population
400 content of the coarse and fine cut-off points within these samples is also near zero (Fig. 10), implying

401 the sediments in this site (Fig. 1a) were deposited from suspension during this time. This is
402 supported by modern sedimentation within the Gulf, where mud (silt and clay) dominates (>95%)
403 the deeper water (> 100 m) parts of the northern continental shelf (Poulos et al., 1996).

404 Weak and dilute flows generated by currents most likely deposited thin and fine-grained
405 sediment layers (mm to <10 cm; e.g., 580.05 mbsf, 589.19 mbsf, 605.09 mbsf, 619.26 mbsf; Fig. 9,
406 b-1 and b-2; Fig. 10). The content of the grain-size population in the range 0.3-0.5 μm from the 540-
407 630 mbsf section fluctuates greatly (except 540-573 mbsf section) compared with that of the 249-
408 323 mbsf section (Fig. 10). A peak (at 259.9 mbsf) in the proportion of 0.3-0.5 μm grains in the 249-
409 323 mbsf section was similar to observations at 540.67mbsf and 565.23 mbsf (Fig. 10), consistent
410 with the grain-size characteristics of event deposits. The fluctuation in the 0.3-0.5 μm grain size
411 component in the 573-630 mbsf section was different from the typical grain-size population of event
412 deposits and from the grain-size population at 0.3-0.5 μm whose content is stable at 0.8% in the
413 249-323 mbsf section. Therefore, the fluctuation of the 0.3-0.5 μm grain size component in the 573-
414 630 mbsf section is interpreted to have been caused by a high-density plume (hydrodynamics 1)
415 derived from fluvial discharge (provenance 2) (as detailed in the next section).

416 On the other hand, the proportion of the grain-size population in the range 0.15-0.25 μm was
417 relatively stable at ca. 10% in the 573-630 mbsf section, while also occasionally reaching 10% in
418 the 249-323 mbsf and 540-573 mbsf sections (the remaining interval content was zero) (Fig. 10).
419 Simultaneously, the population content of the coarse and fine cut-off points show frequent small
420 changes at the same core-depth locations (i.e., where the 0.15-0.25 μm content is at about 10%) (Fig.
421 10). The probability accumulation curves of samples with variations in the 0.15-0.25 μm population

422 content (more than 10%) in the study section were calculated (e.g., 79A-11, 79A-38, 79A-58, 79A-
423 82, 79A-87, 79A-95, 79A-104; Fig. 10), mainly in three-section type and two- section type (Fig.
424 10). The total content of saltation and traction populations accounts for <10% (Fig. 10), clearly
425 distinguishable from the grain-size characteristics of event deposits (Fig. 10). From these results,
426 we have inferred that hyperpycnal flows (hydrodynamics 2) existed in the study area, which derived
427 from fluvial flood discharge (provenance 3) (as detailed in the next section). These inferred
428 hyperpycnal flows may have provided the stable sediment supply in the 573-630 mbsf section, and
429 the intermittent sediment supply in the 249-323 mbsf and 540-573 mbsf sections. The latter
430 hyperpycnal flows from fluvial flood discharge might have been controlled by the current
431 circulation related to the Ishtmia Strait opening.

432 Hydrodynamics and sediment provenance change

433 Fluxes and contributions of main sources to the Gulf of Corinth sediment were complex (e.g., Bell
434 et al., 2009; Nixon et al., 2016; Gawthorpe et al., 2018). In source-to-sink studies for the Corinth
435 rift, Pechlivanidou et al. (2019) argued that the deposited sediments are sands, silts, and clays
436 generated by fluvial erosion of the rift margins for the past 130 ka. Several studies agreed (Collier
437 and Thompson, 1991; Lykousis et al., 2007; Bell et al., 2008; Ford et al., 2016; Gawthorpe et al.,
438 2018) that the sediments may be derived from southern fluvial systems, deltas, gravity deposits,
439 hemipelagic suspension and the flux of sediment from the strait. On the south of the Gulf of Corinth,
440 conglomerate sheets and channel bodies within background sediments of mudstone, siltstone and
441 sandstone are observed in outcrops which expose parts of the Corinth Rift Pleistocene stratigraphy
442 (Gawthorpe et al., 2017). It is thus reasonable that the eastern (including Corinth Isthmus) and

443 central Gulf of Corinth catchments could provide material for the development of hyperpycnal flows
444 and plumes.

445 From Unit 2 onwards, nearly all sedimentation was concentrated in the Gulf and most probably
446 consisted of predominantly fine-grained prodelta facies and hemipelagic deposits (Ford et al., 2016).
447 Several rivers were reversed to a southward flow direction by rapid footwall uplift, starting early in
448 the 700-400 ka time interval (Demoulin et al. 2015), such that the eastern rift is relatively sediment-
449 starved (sediment was supplied from the south by short, consequent rivers; Demoulin et al., 2015),
450 with bathymetry increasing eastwards to over 800 m (Ford et al., 2016). Modern sedimentation
451 within the Gulf is controlled by the input of terrigenous material (by ephemeral rivers and streams
452 along the coastline (Poulos et al., 1996). Hemipelagic processes are associated with biogenic debris
453 from the water column (Poulos et al., 1996) because the biogenic debris includes calcareous algae,
454 benthic foraminifera, ostracods, gastropods, bivalves, dentalium, echinoids and planktonic
455 foraminifera. At the site of M0079A, as can be inferred from the above studies (Fig. 10 and Fig. 11),
456 a stable sediment supply of hemipelagics has operated for the past 700 ka, the suspended load grain-
457 size population tending to be stable, especially since the decrease of river sediment due to drainage
458 reversal (Fig. 11). The hemipelagic deposits (i.e., provenance 1, Fig. 9, c-1 and c-2) are inferred
459 where the 0.3-0.5 μm grain-size population is maintained at 0.8%, and so in the Corinth Rift we
460 interpret this as an index that represents hemipelagic deposition.

461 Cumulative seasonal erosion potential experiments (Leeder et al., 1998) predicted enhanced
462 sediment yields for a cool, wet winter climate during full-glacial climate conditions, and reduced
463 yields for a cool, dry winter climate during interglacial climates. Collier et al. (2000) reported latest

464 Quaternary highstand deposits are distinguished from lowstand Lake Corinth deposits on the basis
465 of seismic reflection data and micropaleontological and palynological analyses of drop cores, and
466 demonstrated enhanced seasonality during the glacial period, with cool, dry summer and wet winter
467 conditions in the Gulf of Corinth. McNeill et al. (2019) reported that the significant increase in
468 sediment fluxes of Lake Corinth during the glacial/isolated periods was confirmed by the IODP
469 core-based sedimentation rates. The above illustrated that rivers maintained effective runoff values
470 of a year during full-glacial conditions because of reduced summer evaporation and increased winter
471 precipitation (Collier et al., 2000). Interglacial conditions were just the opposite. In the site of
472 M0079A, however, little sediment is supplied from the north as no significant rivers flow into the
473 Gulf from the northern coastline (Demoulin et al., 2015; Gawthorpe et al, 2018) and mainly fine-
474 grained sediment is supplied from the south by short, consequent rivers (Demoulin et al., 2015; Ford
475 et al., 2016). It is interpreted that the eastern and central Gulf of Corinth had a stable higher fluvial
476 sediment contribution before drainage reversal (when there were larger catchments in the rift
477 footwall), and then the fluvial sediment flux decreased significantly.

478 Along the southern margin of the Corinth rift, Poulos et al. (1996) suggested that gravity-driven
479 mass flows are often generated often by high fluvial sediment contributions from seasonal rivers or
480 freshwater flood events. Bates (1953) and others (Mulder and Syvitski, 1995; Mulder et al., 2003)
481 indicated that the high-density plumes triggered by river floods generate hyperpycnal flows. Piper
482 et al. (1988) also indicated that the fine sediment reaching the basin floor (Gulf of Corinth) appears
483 derived mainly from muddy plumes during winter floods. These studies revealed that fluvial
484 sediments could be transported to the basin floor during flood events. This was supported by recent

485 research within the Gulf (Maffione and Herrero-Bervera, 2022), recognizing that the variability in
486 grain-size may have been related to the variable intensity of bottom currents in the rift basin.

487 In addition, Ford et al. (2016) built a model of the westwards propagation and northwards
488 migration of the rift since the Pleistocene, and a recent deepening event that occurred in the central
489 Gulf of Corinth at approximately 400 ka. This deepening event was similar to the understanding of
490 some workers (Lykousis et al., 2007) in which the present-day depth of the central Gulf of Corinth
491 seafloor (870 m) could be the result of a continuous deepening of the basin during the last 500 ka.
492 These show that the water depth of hole M0079A deepens since ca. 400-500 ka.

493 The above studies imply a relatively sustained sediment supply from rivers (i.e., high-density
494 plumes) during the interval 700 ka to circa 500-400 ka. Since circa 400-500 ka, fluvial sediments
495 were transported to the study area during floods (i.e., as hyperpycnal flows) during the continuous
496 deepening of the basin. The variation of sediment supply from rivers is denoted by the variation in
497 the 0.15-0.25 μm population component (Fig. 11) (i.e., provenance 2, fluvial discharge;
498 hydrodynamics 1, high-density plume in the 573-630 mbsf section; and provenance 3, fluvial flood
499 discharge; hydrodynamics 2, hyperpycnal flows in the 249-323 mbsf and 540-573 mbsf section).

500 The reasons for the significant changes in the content characteristics of the grain-size
501 population at 0.15-0.25 μm and 0.3-0.5 μm in the section above and below 573 mbsf (ca. 593-613
502 ka) were as follows: (1) several rivers were reversed by rapid uplift starting at the beginning of the
503 700-400 ka interval (Demoulin et al. 2015), (2) fine-grained sediment was supplied from the south
504 by short, consequent rivers since circa 500-400 ka (Demoulin et al., 2015; Ford et al., 2016), (3) the
505 westwards propagation and northwards migration of the rift since the Pleistocene (Ford et al., 2016),

506 a continuous deepening of the basin during the last 500 ka (Lykousis et al., 2007), and (4) structural
507 subsidence and opening of straits through the pre-existing land barriers at the eastern (Corinth
508 Isthmus) and/or western (Rion Sill) end of the Corinth Rift since approximately 0.6 Ma (i.e., the
509 "Great Breaching" of Gawthorpe et al, 2018).

510 The main grain-size characteristics that allow provenance and hydrodynamic identification in
511 this area were obtained by combining provenance, hydrodynamic analysis, probability accumulation
512 curve and grain-size populations (Fig. 12). These may be distinguished as: (1) The probability
513 accumulation curve of event deposits (possibly earthquake-triggered) has three-section type
514 characteristics, with the proportion of coarse particles ($<4.5 \phi$) close to or more than 50%, and the
515 proportion of the total content of saltation and traction populations more than 20%. (2) The
516 probability accumulation curve of hyperpycnal flows and high-density plumes has two-section type
517 and three-section type characteristics, with the proportion of coarse particles ($<4.5 \phi$) basically
518 between 5% and 30%. The total content of saltation and traction populations accounts for $<10\%$ of
519 the total population. (3) The probability accumulation curve of hemipelagic deposits has zero-
520 section type and one-section type characteristics, with the proportion of the finer-grained particles
521 ($>3 \phi$) being more than 99%.

522 Central basin Late Pleistocene rift sediments recording the presence of straits
523 We integrate our new hydrodynamic and provenance information from the site of M0079A with
524 published sedimentological, hydrological and new age interpretations (Maffione and Herrero-
525 Bervera, 2022) to develop a model of the sediment supply to the site of M0079A in no-strait versus
526 open strait states during the Late Pleistocene. The two main environmental phases of development
527 correspond approximately to those recognized in the recent work in the central Gulf of Corinth

528 (Nixon et al., 2016; Gawthorpe et al., 2018, McNeil et al., 2019; Gawthorpe et al., 2022):

529 An isolated lake with intermittent marine incursions existed from ca. 0.7 to 0.613-0.593 Ma.
530 The main rivers of the southern catchments maintained a northward course (Fig. 1), and the site of
531 M0079A had a stable high fluvial sediment contribution (Fig. 13b). Slumps, as isolated beds were
532 observed in cores (Fig. 9 a-1 and a-2), indicating slopes around the site of M0079A were unstable
533 (Fig. 13b). The deposits of high-density plumes were deposited here during this period, and
534 accompanying slumps may have been earthquake-triggered (Sachpazi et al., 2003). At this time the
535 presence of structural sills/land barriers at the eastern (Corinth Isthmus) and western (Rion Straits)
536 ends of the main depocentre confined the lacustrine rift (Bell et al., 2008; Gawthorpe et al., 2018).
537 The supply of suspended sediments was substantially derived from low-density plumes (including
538 lofted plumes, Gawthorpe et al., 2022; Fig. 13b), with small amounts derived from hemipelagic
539 suspension.

540 The main Corinth Rift depocentre was periodically sea-connected from ca. 0.613-0.593 to
541 0.168 Ma. The westwards propagation and northwards migration of the rift (Ford et al., 2016), cause
542 the migration of the depocenter of the rift basin (with the deepest basin floor in the basin axis near
543 the site of M0079A; Fig. 1; Fig. 13a). The main rivers were reversed (Fig. 1a), reducing fluvial
544 sediment supply to the central and eastern parts of the rift. Slumps representing slope collapse
545 deposits were not observed in cores, suggesting such deposits were trapped close to the rift margins
546 (Fig. 13a). The deposits of this period commonly consisted of turbidites supplied by hyperpycnal
547 flow during rivers flood events (Piper et al., 1988; Maffione and Herrero-Bervera, 2022), turbidity
548 currents that may have been earthquake-triggered (Sachpazi et al., 2003), and the delivery of

549 sediment from cascading strait currents off the shelf (Collier and Thompson, 1991).

550 Structural or erosional control of land barriers at the eastern (Corinth Isthmus) and/or western
551 (Rion Sill) ends of the rift allowed initial marine incursion around 0.6 Ma (i.e., the "Great
552 Breaching" of Gawthorpe et al, 2018). The sediments of shallow marine in the stratigraphic section
553 exposed by the excavation of the Corinth Canal provide evidence for the episodic existence of a
554 strait through much of the Late Pleistocene (Collier, 1990; Fig. 13c). Moreover, the distribution of
555 transverse and linear dunes in the Corinth Basin suggest that a strait periodically existed across the
556 Corinth Isthmus during the Late Pleistocene (Collier and Thompson, 1991). The oldest marine
557 sediments exposed in the canal section occur above and then alternate with the white and grey
558 Corinth Marls (Fig. 13c). The expression of fluctuating relative sea level on one coastline of the
559 Isthmus strait during this time is exemplified by the prominent karstification of a marl surface, due
560 to a relative base-level fall (Collier, 1990). The marl is capped by a beach/shoreface transgressive
561 to progradational package associated with glacio-eustatic marine transgression at ca. 0.4 Ma. Fig.
562 13d illustrates bidirectional ripples indicating tidal influence in this shallow marine environment.
563 Tidal dune bedforms also developed within the strait during a younger glacio-eustatic transgression,
564 as described by Collier & Thompson (1991). After each glacio-eustatic highstand, the Gulf of
565 Corinth was cut off again from open marine conditions due to a relative base-level fall below the
566 level of the Corinth Isthmus structural sill (Fig. 13c). Cycles of transgression and base-level fall,
567 alternating between open and closed strait conditions, were repeated ca. every 100 ka until the
568 Corinth Isthmus permanently emerged above sea-level (Collier, 1990), by which time marine
569 connection during glacio-eustatic highstands was established at the western end of the rift

570 (Somerville et al., 2019; Gawthorpe et al., 2022).

571 The core from the IODP borehole M0079A was collected some 10-20 km away from the
572 Isthmia paleo-strait and associated strait currents that would have been focused through the strait
573 during phases of relatively high sea level (Collier and Thompson, 1991). The “far field strait effect”
574 formed by the Gulf of Corinth being periodically sea-connected might have led suspended sediments
575 to have been mainly derived from hemipelagic suspension, from more distal the low-density plumes
576 (Fig. 13a). However, our analysis of the deep-water core material shows the deposits got coarser
577 during the connected (marine water) intervals (Figs. 3 and 4). This observation together with the
578 reconstruction of the Isthmia area (Collier and Thompson, 1991) suggests that strait-related currents
579 from the Isthmus strait likely promoted the transport of shallow water sediments into the main
580 Corinth Rift axial depocenter from the shallower shelf. Collier and Thompson (1991) reconstructed
581 a shallow platform in the SE part of the Gulf of Corinth basin where currents were large enough to
582 form large bedforms. It was likely the strait currents were circulating in a clockwise pattern and
583 were cascading off the shallow platform to deeper water, depositing coarser grained sediments and
584 facilitating bioturbation (higher oxygen content waters). The water circulation through the
585 structurally controlled strait and its connectivity with deep water (Fig. 13a) might explain the coarser
586 grained deposits during accumulation of the marine deposits (Figs. 3 and 4).

587 Conclusions

588 The sedimentary environments of the Gulf of Corinth changed from an isolated lake, with
589 intermittent marine incursions (before ca. 0.593-0.613 Ma, namely 570.51 mbsf to 577.00 mbsf), to
590 a gulf periodically sea-connected (after ca. 0.593-0.613 Ma). In the 573-630 mbsf section, sediments

591 were mainly derived from long rivers on the southern margin of the Corinth Rift and the fluvial-
592 sourced sediments were transported by high-density plumes and intervening hemipelagic deposition
593 by suspension settling. Due to drainage reversals at circa 0.593-0.613 Ma, in the 249-323 mbsf and
594 540-573 mbsf section, the sediments were mainly derived from hemipelagic settling and
595 hyperpycnal flows during river (short, consequent river) flood events. Many event deposits in the
596 study section may have been earthquake-triggered.

597 The 0.15-0.25 μm component of the grain-size population of the sediments in the study area
598 (i.e., from site M0079A) was mainly deposited through hyperpycnal flows since 0.593-0.613 Ma,
599 triggered by river floods on the southern margin of the Corinth Rift. The variation of the population
600 content of 0.15-0.25 μm implies periodic floods. When sediment was supplied from hemipelagic
601 deposition, the proportion of the grain-size population in the range 0.3-0.5 μm was maintained at
602 0.8%, which is an index that represents suspension fall-out deposits laid down under extremely low-
603 energy conditions. Before 0.593-0.613 Ma, the 0.15-0.25 μm component of grain-size population
604 of sediments indicates deposition out of more stable high-density plumes, sourced not far from the
605 study area.

606 A probability accumulation curve chart was established to distinguish hemipelagic deposits,
607 event deposits (possibly earthquake-triggered), hyperpycnal flows and high-density plumes in the
608 Gulf of Corinth. This approach may be found useful in the characterization of fine-grained
609 sediments in other deep-water settings. The deep-water sediments of the M0079A borehole record
610 more frequent coarser beds during the marine periods when the Isthmia Strait was open. The
611 presence of the open strait likely changed the shallow water current circulation in the SE area of the

612 basin and promoted delivery of shallow sediments to the deep-water basin axis.

613

614 **Acknowledgments:** We sincerely thank all involved with the successful completion of IODP
615 Expedition 381, including ECORD Science Operator staff, ship and drilling crew of the D/V Fugro
616 Synergy, and staff at MARUM, University of Bremen. We thank the Natural Science Foundation
617 of China, Fundamental Research Funds for the Central Universities and IODP Expedition 381
618 provided support. We are thankful to Dr. Olariu and Dr. Rossi for editorial guidance and reviewers
619 for insightful reviews that improved the manuscript.

620 **Funding:** This study was supported by the Natural Science Foundation of China, China
621 (42272124, 41802129), the Fundamental Research Funds for the Central Universities, China (2-9-
622 2019-100), and IODP Expedition 381.

623 **Data availability:** All data and material pertinent to this study are contained within the
624 manuscript and Supplementary Information, and/or the IODP Expedition 381 Preliminary Report.
625 The full dataset from IODP Expedition 381 will become openly available on March 1, 2019, via the
626 IODP website (<https://www.iodp.org/resources/access-data-and-samples>), including access to core
627 materials and logging data.

628 **References**

- 629 [1] Abrahamsson, K., Granfors, A., Ahnoff, M. Cuevas, C.A. and Saiz-Lopez, A. 2018. Organic bromine
630 compounds produced in sea ice in Antarctic winter. Nat Commun 9, 5291, [https://doi.org/10.1038/s41467-018-](https://doi.org/10.1038/s41467-018-07062-8)
631 [07062-8](https://doi.org/10.1038/s41467-018-07062-8)
- 632 [2] Allen, P.A., Michael, N.A., D'Arcy, M., Roda-Boluda, D.C., Whittaker, A.C., Duller, R.A. and Armitage, J.J.

- 633 2016. Fractionation of grain-size in terrestrial sediment routing systems. *Basin Research*, 29, 180-202,
634 <https://doi.org/10.1111/bre.12172>
- 635 [3] Backert, N., Ford, M. and Malartre, F. 2010. Architecture and sedimentology of the Kerinitis Gilbert-type fan
636 delta, Corinth Rift, Greece. *Sedimentology*, 57, 543-586, <https://doi.org/10.1111/j.1365-3091.2009.01105.x>
- 637 [4] Bates, C.C. 1953. Rational theory of delta formation. *AAPG Bulletin*, 37, 2119-2126, [https://doi.org/](https://doi.org/10.1306/5CEADD76-16BB-11D7-8645000102C1865D)
638 [10.1306/5CEADD76-16BB-11D7-8645000102C1865D](https://doi.org/10.1306/5CEADD76-16BB-11D7-8645000102C1865D)
- 639 [5] Beelen, D., Wood, L.J, Zaghoul, M.N., Cardona, C. and Arts, M. 2022. Channel, dune and sand sheet
640 architectures of a strait-adjacent delta, Rifian Corridor, Morocco. *Geological Society, London, Special Publications*, 523, <https://doi.org/10.1144/SP523-2021-49>
- 641
- 642 [6] Bell, R.E., McNeill, L.C., Bull, J.M., Henstock, T.J., Collier, R.E.L. and Leeder, M.R. 2009. Fault architecture,
643 basin structure and evolution of the Gulf of Corinth Rift, central Greece. *Basin Research*, 21, 824-855,
644 <https://doi.org/10.1111/j.1365-2117.2009.00401.x>
- 645 [7] Bell, R.E., McNeill, L.C., Bull, J.M. and Henstock, T.J. 2008. Evolution of the offshore western Gulf of Corinth.
646 *Geological Society of America Bulletin*, 120, 156-178, <https://doi.org/10.1130/B26212.1>
- 647 [8] Bernard, P., Lyon-Caen, H., Briole, P., Deschamps, A., Boudin, F., Makropoulos, K., Papadimitriou, P.,
648 Lemeille, F., Patau, G., Billiris, H., Paradissis, D., Papazissi, K., Castarede, H., Charade, O., Necessian, A.,
649 Avallone, A., Pacchiani, F., Zahradnik, J., Sacks, S. and Linde, A. 2006. Seismicity, deformation and seismic
650 hazard in the western rift of Corinth: new insights from the Corinth Rift Laboratory (crl). *Tectonophysics*, 426,
651 7-30, <https://doi.org/10.1016/j.tecto.2006.02.012>
- 652 [9] Bickle, M.J., Chapman, H.J., Bunbury, J., Harris, N.B.W., Fairchild, I.J., Ahmad, T. and Pomiès, C. 2005. The
653 Relative Contributions of Silicate and Carbonate Rocks to Riverine Sr Fluxes in the Head Waters of the Ganges.

- 654 Geochimica et Cosmochimica Acta, 69(9): 2221-2240, <https://doi.org/10.1016/j.gca.2004.11.019>
- 655 [10] Briole, P., Rigo, A., Lyon-Caen, H., Ruegg, J.C. and Deschamps, A. 2000. Active deformation of the Corinth
656 rift, Greece: results from repeated global positioning system surveys between 1990 and 1995. Journal of
657 Geophysical Research, 105, 25605-25626, <https://doi.org/10.1029/2000JB900148>
- 658 [11] Bui, E.N., Loeppert, R.H. and Wilding, L.P. 1990. Carbonate phases in calcareous soils of the weste
659 rn united states. Soil Science Society of America Journal, 54, 39-45, [https://doi.org/10.2136/sssaj1990.
660 03615995005400010006x](https://doi.org/10.2136/sssaj1990.03615995005400010006x)
- 661 [12] Caley, T., Malaizé, B., Zaragosi, S., Rossignol, L., Bourget, J., Eynaud, F., Martinez, P., Giraudeau, J., Charlier,
662 K. and Ellouz-Zimmermann, N. 2011. New Arabian Sea records help decipher orbital timing of indo-Asian
663 monsoon. Earth & Planetary Science Letters, 308, 433-444, <https://doi.org/10.1016/j.epsl.2011.06.019>
- 664 [13] Campos, C., Beck, C., Crouzet, C., Carrillo, E. and Tripsanas, E. 2013. Late Quaternary paleoseismic
665 sedimentary archive from deep central Gulf of Corinth: time distribution of inferred earthquake-induced layers.
666 Annals of Geophysics, 56, S0670, <https://doi.org/10.4401/ag-6226>
- 667 [14] Cavazza, W. and Longhitano, S.G. 2022. Palaeostrait tectonosedimentary facies during late Cenozoic
668 microplate rifting and dispersal in the western Mediterranean. Geological Society, London, Special
669 Publications, 523, <https://doi.org/10.1144/SP523-2021-95>
- 670 [15] Clarke, P.J., Davies, R.R., England, P.C., Parsons, B., Billiris, H., Paradissis, D., Veis, G., Cross, A., Denys,
671 P.H., Ashkenazi, V., Bingley, R., Kahle, H.G., Muller, M.V. and Briole, P. 1998. Crustal strain in central Greece
672 from repeated GPS measurements in the interval 1989–1997. Geophysical Journal International, 135, 195-214,
673 <https://doi.org/10.1046/j.1365-246X.1998.00633.x>
- 674 [16] Collier, R.E.L.L. 1990. Eustatic and tectonic controls upon Quaternary coastal sedimentation in the Corinth

- 675 Basin, Greece. Journal of the Geological Society, 147, 301-314, <https://doi.org/10.1144/gsjgs.147.2.0301>
- 676 [17] Collier, R.E.L. and Dart, C.J. 1991. Neogene to quaternary rifting, sedimentation and uplift in the Corinth
677 Basin, Greece. Journal of the Geological Society, 148, 1049-1065, <https://doi.org/10.1144/gsjgs.148.6.1049>
- 678 [18] Collier, R.E.L. and Thompson, J. 1991. Transverse and linear dunes in an upper Pleistocene marine sequence,
679 Corinth Basin, Greece. Sedimentology, 38, 1021-1040, <https://doi.org/10.1111/j.1365-3091.1991.tb00369.x>
- 680 [19] Collier, R.E.L., Leeder, M.R., Trout, M., Ferentinos, G., Lyberis, E. and Papatheodorou, G. 2000. H
681 igh sediment yields and cool, wet winters: Test of last glacial paleoclimates in the northern Mediterr
682 anean. Geology, 28, 999-1002, [https://doi.org/10.1130/0091-7613\(2000\)28<999:HSYACW>2.0.CO;2](https://doi.org/10.1130/0091-7613(2000)28<999:HSYACW>2.0.CO;2)
- 683 [20] Demoulin, A., Beckers, A. and Hubert-Ferrari, A. 2015. Patterns of Quaternary uplift of the Corinth rift
684 southern border (N Peloponnese, Greece) revealed by fluvial landscape morphometry. Geomorphology, 246,
685 188-204, <https://doi.org/10.1016/j.geomorph.2015.05.032>
- 686 [21] Ding, Z.L., Han, J.T., Liu, C., Liu, D.S. and Liu, T.S. 1991. Preliminary determination of an abrupt climatic
687 shift around 2.5 Ma in northern China (eng). Chinese Science Bulletin, 36, 852-852,
688 <https://doi.org/10.1288/00005537-196101000-00010>
- 689 [22] Evans, J.N., McIlroy, D. and Smith, A. 2019. Ichnology and palaeobiology of phoebichnus trochoides from the
690 middle Jurassic of north-east England. Papers in Palaeontology, 2, 139-154, <https://doi.org/10.1002/spp2.1035>
- 691 [23] Folk, R.L. and Ward, W.C. 1957. Brazos River bar: a study in the significance of grain-size parameters. Journal
692 of Sedimentary Research, 27, 3-26, <https://doi.org/10.1306/74D70646-2B21-11D7-8648000102C1865D>
- 693 [24] Ford, M., Hemelsdal, R., Mancini, M. and Palyvos, N. 2016. Rift migration and lateral propagation: evolution
694 of normal faults and sediment-routing systems of the western Corinth rift (Greece). Geological Society,
695 London, Special Publications, SP439, 15, <http://doi.org/10.1144/SP439.15>

- 696 [25] Ford, M., Williams, E.A., Malartre, F. and Popescu, S.M., 2007. Stratigraphic architecture, sedimentology and
697 structure of the Vouraikos Gilbert-type fan delta, Gulf of Corinth, Greece. *Sedimentary Processes,*
698 *Environments and Basins: A Tribute to Peter Friend*, 38, 49-90, <https://doi.org/10.1002/9781444304411.ch4>
- 699 [26] Ford, M., Rohais, S., Williams, E.A., Bourlange, S., Jousselin, D., Backert, N. and Malartre, F. 2013. Tectono-
700 sedimentary evolution of the western Corinth rift (central Greece). *Basin Research*, 25, 3-25,
701 <https://doi.org/10.1111/j.1365-2117.2012.00550.x>
- 702 [27] Friedman, G.M. 1967. Dynamic processes and statistical parameters compared for size frequency distribution
703 of beach and river sands. *Journal of Sedimentary Research*, 37, 327-354, [https://doi.org/10.1306/74D716CC-](https://doi.org/10.1306/74D716CC-2B21-11D7-8648000102C1865D)
704 [2B21-11D7-8648000102C1865D](https://doi.org/10.1306/74D716CC-2B21-11D7-8648000102C1865D)
- 705 [28] Fuller, A.O. 1961. Size distribution characteristics of shallow marine sands from the cape of good hope, south
706 Africa. *Journal of Sedimentary Research*, 31, 256-261, [https://doi.org/10.1306/74D70B4B-2B21-11D7-](https://doi.org/10.1306/74D70B4B-2B21-11D7-8648000102C1865D)
707 [8648000102C1865D](https://doi.org/10.1306/74D70B4B-2B21-11D7-8648000102C1865D)
- 708 [29] Gamboa, A., Montero-Serrano, J., St-Onge, G., Rochon, A. and Desiagne, P. 2017. Mineralogical, geochemical,
709 and magnetic signatures of surface sediments from the Canadian Beaufort Shelf and Amundsen Gulf (Canadian
710 Arctic). *Geochemistry Geophysics Geosystems*, 18, 488-512, <https://doi.org/10.1002/2016GC006477>
- 711 [30] Ganti, V., Lamb, M. P. and McElroy, B. 2014. Quantitative bounds on morphodynamics and implications for
712 reading the sedimentary record. *Nature Communications*, 5, 3298, https://doi.org/10.1038/ncomm_s4298
- 713 [31] Gao, S. and Collins M.B. 1994. Analysis of grain-size trends, for defining sediment transport pathways in
714 marine environments. *Journal of Coastal Research*, 10: 70-78, <https://www.jstor.org/stable/4298194>
- 715 [32] Gawthorpe, R.L., Andrews, J.E., Collier, R., Ford, M. and Skourtsos, E. 2017. Building up or out?
716 disparate sequence architectures along an active rift margin—Corinth rift, Greece. *Geology*, 45, 1111-

- 717 1114, <https://doi.org/10.1130/G39660.1>
- 718 [33] Gawthorpe, R.L., Leeder, M.R., Kranis, H., Skourtsos, E., Andrews, J.E., Henstra, G.A., Mack, G.H.,
719 Muravchik, M., Turner, J.A. and Stamatakis, M. 2018. Tectono-sedimentary evolution of the Plio-Pleistocene
720 Corinth rift, Greece. *Basin Research*, 30, 448-479, <https://doi.org/10.1111/bre.12260>
- 721 [34] Gawthorpe, R.L., Fabregas, N., Pechlivanidou, S., Ford, M., Collier, R.E.L., Carter, G.D.O., McNeill, L.C.
722 and Shillington, D.J. 2022. Late Quaternary mud-dominated, basin-floor sedimentation of the Gulf of Corinth,
723 Greece: Implications for deep-water depositional processes and controls on syn-rift sedimentation. *Basin*
724 *Research, Online*, 1-34, <https://doi.org/10.1111/bre.12671>
- 725 [35] Grabau, A.W., 1904. Phylogeny of *Fusus* and its allies. *Smithsonian Miscellaneous Collections*, 44, 1-157.
- 726 [36] Gelder, G.D., Mai, L.D., Beck, C., Carlut, J., Seibert, C., N Feuillet, N., D.O. Carter, G., Pechlivanidou, S. and
727 L.Gawthorpe, R. 2021. Multi-scale and multi-parametric analysis of Late Quaternary event deposits within the
728 active Corinth Rift (Greece). *Sedimentology*, 69, 1573-1598, <https://doi.org/10.1111/sed.12964>
- 729 [37] Heezen, B.C., Ewing, M. and Johnson, G.L., 1966. The Gulf of Corinth floor. *Deep Sea Research and*
730 *Oceanographic Abstracts*, 13, 381-411, [https://doi.org/10.1016/0011-7471\(66\)91076-X](https://doi.org/10.1016/0011-7471(66)91076-X)
- 731 [38] Hussain, A., Haughton, P.D.W., Shannon, P.M., Turner, J.N., Pierce, C.S., Obradors-Latre, A., Barker, S.P. and
732 Martinsen, O.J. 2020. High-resolution X-ray fluorescence profiling of hybrid event beds: Implications for
733 sediment gravity flow behaviour and deposit structure. *Sedimentology*, 67, 2850-2882,
734 <https://doi.org/10.1111/sed.12722>
- 735 [39] Hussain, A., Butt, M.N., Olariu, C., Malik, M.H., Koeshidayatullah, A., Amao, A. and Al-Ramadan, K. 2022.
736 Unravelling reservoir quality heterogeneity in mixed siliciclastic-carbonate deposits: An example from
737 Miocene Red Sea rift, NW Saudi Arabia. *Marine and Petroleum Geology*, 145,

- 738 <https://doi.org/10.1016/j.marpetgeo.2022.105850>.
- 739 [40] Jiang Z.X. 2010. Sedimentology (in Chinese with English abstract). Petroleum Industry Press, Beijing, pp.
740 237-243.
- 741 [41] Kanhaiya, S., Singh, B.P., Tripathi, M., Sahu, S. and Tiwari, V. 2016. Lithofacies and particle-size
742 characteristics of late quaternary floodplain deposits along the middle reaches of the Ganga river, central Ganga
743 plain, India. *Geomorphology*, 284, 220-228, <https://doi.org/10.1016/j.geomorph.2016.08.030>
- 744 [42] Kontopoulos, N. and Avramidis, P. 2003. A late Holocene record of environmental changes from the Aliko
745 lagoon, Egion, North Peloponnesus, Greece. *Quaternary International*, 111, 75-90,
746 [https://doi.org/10.1016/S1040-6182\(03\)00016-8](https://doi.org/10.1016/S1040-6182(03)00016-8)
- 747 [43] Krumbein, W.C. and Pettijohn, F.J. 1938. Manual of sedimentary petrography. Appleton-Century-Crofts, Inc.
748 New York. 544.
- 749 [44] Krumbein, W.C. 1934. Size frequency distributions of sediments. *Journal of Sedimentary Research*, 4, 65-77,
750 <https://doi.org/10.1306/D4268EB9-2B26-11D7-8648000102C1865D>
- 751 [45] Lane, E.W. 1938. Notes on the formation of sand. *Eos, Transactions American Geophysical Union*, 19, 505-
752 508, <https://doi.org/10.1029/TR019i001p00505>
- 753 [46] Lea, D.W., Pak, D.K. and Spero, H.J. 2000. Climate impact of late quaternary equatorial pacific sea surface
754 temperature variations. *Science*. 289, 1719-1724, <https://doi.org/10.1126/science.289.5485.1719>
- 755 [47] Leeder, M.R., Harris, T. and Kirkby, M.J. 1998. Sediment supply and climate change: Implications for basin
756 stratigraphy. *Basin Research*, 10, 7-18, <https://doi.org/10.1046/j.1365-2117.1998.00054.x>
- 757 [48] Leeder, M.R., Mack, G.H., Brasier, A.T., Parrish, R.R., McIntosh, W.C., Andrews, J.E. and Duermeijer, C.E.
758 2008. Late-Pliocene timing of Corinth (Greece) rift-margin fault migration. *Earth and Planetary Science*

- 759 Letters, 274, 132-141, <https://doi.org/10.1016/j.epsl.2008.07.006>
- 760 [49] Leeder, M.R., Mark, D.F., Gawthorpe, R.L., Kranis, H., Loveless, S., Pedentchouk, N., Skourtsos, E., Turner,
761 J., Andrews, J.E. and Stamatakis, M. 2012. A “Great Deepening”: Chronology of rift climax, Corinth Rift,
762 Greece. *Geology*, 40(11), 999-1002, <https://doi.org/10.1130/G33360.1>
- 763 [50] Li, S., Yu, X., Steel, R., Zhu, X., Li, S., Cao, B. and Hou, G. 2018. Change from tide-influenced deltas in a
764 regression-dominated set of sequences to tide-dominated estuaries in a transgression-dominated sequence set,
765 East China Sea Shelf Basin. *Sedimentology*, 65, 2312-2338, <https://doi.org/10.1111/sed.12466>
- 766 [51] Lin, C.M., Zhu, H.C., Gao, S. 2005. Sedimentary facies and evolution in the Qiantang River incised valley,
767 eastern China. *Marine Geology*, 219, pp. 235-259, <https://doi.org/10.1016/j.margeo.2005.06.009>.
- 768 [52] Lu, S.Q., Wang, J. and Cao, Y.C. 2013. Study on characteristics and hydrodynamic significance of grain-size
769 components of beach-bar sandbodies, second member of Shahejie formation, Chexi sag (in Chinese with
770 English abstract). *Petroleum Geology & Recovery Efficiency*, 20, 26-29.
- 771 [53] Lykousis, V., Sakellariou, D., Moretti, I. and Kaberi, H., 2007. Late quaternary basin evolution of the Gulf of
772 Corinth: Sequence stratigraphy, sedimentation, fault–slip and subsidence rates. *Tectonophysics*, 440, 29-51,
773 <https://doi.org/10.1016/j.tecto.2006.11.007>
- 774 [54] Malcolm, S.J. and Price, N.B. 1984. The behavior of iodine and bromine in estuarine surface sediments. *Marine*
775 *Chemistry*, 15, 263-271, [https://doi.org/10.1016/0304-4203\(84\)90022-7](https://doi.org/10.1016/0304-4203(84)90022-7)
- 776 [55] Mangini, A., Eisenhauer, A. and Walter, P. 1990. Response of manganese in the ocean to the climatic cycles in
777 the Quaternary. *Paleoceanography*, 5(5): 811-821, <https://doi.org/10.1029/PA005i005p00811>
- 778 [56] Mason, C.C. and Folk, R.L. 1958. Differentiation of beach, dune, and aeolian flat environments by size analysis,
779 mustang island, Texas. *Journal of Sedimentary Research*, 28, 211-226, <https://doi.org/10.1306/74D707B3->

- 780 [2B21-11D7-8648000102C1865D](https://doi.org/10.1007/s12594-015-0332-2)
- 781 [57] Maffione, M. and Herrero-Bervera, E. 2022. A relative paleointensity (RPI)-calibrated age model for the
782 Corinth syn-rift sequence at IODP Hole M0079A (Gulf of Corinth, Greece). *Frontiers in Earth Science*, 10,
783 <https://doi.org/10.3389/feart.2022.813958>
- 784 [58] McLaren, P. and Bowles, D. 1985. The effects of sediment transport on grain-size distributions. *Journal of*
785 *Sedimentary Research*, 55, 457-470, <https://doi.org/10.1306/212F86FC-2B24-11D7-8648000102C1865D>
- 786 [59] McManus, J. 1988. Grain-size determination and interpretation. In: Tucker(ed). *Techniques in Sedimentology*.
787 Oxford: Blackwell. pp. 63-85.
- 788 [60] McNeill, L.C., Cotterill, C.J., Henstock, T.J., Bull, J.M., Stefatos, A., Collier, R., Papatheoderou, G., Ferentinos,
789 G. and Hicks, S.E. 2005. Active faulting within the offshore western Gulf of Corinth, Greece: Implications for
790 models of continental rift deformation. *Geology*, 33, 241-244, <https://doi.org/10.1130/G21127.1>
- 791 [61] McNeill, L.C., Shillington, D.J., Carter, G.D.O., Everest, J.D., Gawthorpe, R.L., Miller, C., Phillips, M.P.,
792 Collier, R.E.L., Cvetkorpe, A., Gelder, G.D., Diz, P., Doan, M.L., Ford, M., Geraga, M., Gillespie, J.,
793 Hemelsdael, R., Herrero-Bervera, E., Ismaiel, M., Janikian, L., Kouli, K., Ber, E.L., Li, S.L., Maffione, M.,
794 Mahoney, C., Machlus, M.L., Michas G., Nixon, C.W., Oflaz, S.A., Omale, A.P., Panagiotopoulos, K.,
795 Pechlivanidou, S., Sauer, S., Seguin, J., Sergiou, S., Zakharova, N.V. and Green, S. 2019. High-resolution
796 record reveals climate-driven environmental and sedimentary changes in an active rift. *Scientific Reports*, 9,
797 6519, <https://doi.org/10.1038/s41598-019-42749-y>
- 798 [62] Mir, R.A. and Jeelani, G. 2015. Textural characteristics of sediments and weathering in the Jhelum river basin
799 located in Kashmir valley, western Himalaya. *Journal of the Geological Society of India*, 86, 445-458,
800 <https://doi.org/10.1007/s12594-015-0332-2>

- 801 [63] Moretti, I., Lykousis, V., Sakellariou, D., Reynaud, J.Y., Benziane, B. and Prinzoffer, A. 2004. Sedimentation
802 and subsidence rate in the Gulf of Corinth: what we learn from the marion dufresne's long-piston coring.
803 Comptes Rendus Geoscience, 336, 291-299, <https://doi.org/10.1016/j.crte.2003.11.011>
- 804 [64] Mulder, T. and Syvitski, J.P.M. 1995. Turbidity currents generated at river mouths during exceptional
805 discharges to the world oceans. Journal of Geology, 103, 285-299, <https://doi.org/10.1086/629747>
- 806 [65] Mulder, T., Syvitski, J.P.M., Migeon, S., Faugères, J.C. and Savoye, B. 2003. Marine hyperpycnal flows:
807 initiation, behavior and related deposits. A review. Marine and Petroleum Geology, 20, 861-882,
808 <https://doi.org/10.1016/j.marpetgeo.2003.01.003>
- 809 [66] Nixon, C.W., McNeill, L.C., Bull, J.M., Bell, R.E., Gawthorpe, R.L., Henstock, T.J., Christodoulou, D., Ford,
810 M., Taylor, B., Sakellariou, D., Ferentinos, G., Papatheodorou, G., Leeder, M.R., Collier, R.E.L., Goodliffe,
811 A.M., Sachpazi, M. and Kranis, H. 2016. Rapid spatiotemporal variations in rift structure during development
812 of the Corinth Rift, central Greece. Tectonics, 35, 1225-1248, <https://doi.org/10.1002/2015TC004026>
- 813 [67] Nizou, J., Hanebuth, T., Heslop, D., Schwenk, T., Palamenghi, L., Stuut, J.B. and Henrich, R. 2010. The
814 Senegal River mud belt: A high-resolution archive of paleoclimatic change and coastal evolution. Marine
815 Geology, 278, 150-164, <https://doi.org/10.1016/j.margeo.2010.10.002>
- 816 [68] Nomikou, P., Alexandri, M., Lykousis, V., Sakellariou, D. and Ballas, D. 2011. Swath bathymetry and
817 morphological slope analysis of the Corinth Gulf. Quaternary International, 155-158.
- 818 [69] Otto, G.H. 1939. A Modified Logarithmic Probability Graph for the Interpretation of Mechanical Analyses of
819 Sediments. Journal of Sedimentary Petrology, 9, 62-76, [https://doi.org/10.1306/D4269044-2B26-11D7-
820 8648000102C1865D](https://doi.org/10.1306/D4269044-2B26-11D7-8648000102C1865D)
- 821 [70] Passega, R. 1957. Texture as characteristic of clastic deposition. AAPG Bulletin, 41, 1952-1984,

- 822 <https://doi.org/10.1306/0BDA594E-16BD-11D7-8645000102C1865D>
- 823 [71] Pechlivanidou, S., Cowie, P.A., Hannisdal, B., Whittaker, A.C., Gawthorpe, R.L., Pennos, C. and Riiser, O.S.
824 2018. Source-to-sink analysis in an active extensional setting: Holocene erosion and deposition in the
825 Sperchios rift, central Greece. *Basin Research*, 30, 522-543, <https://doi.org/10.1111/bre.12263>
- 826 [72] Pechlivanidou, S., Cowie, P.A., Duclaux, G., Nixon, C.W. and Salles, T. 2019. Tipping the balance: shifts in
827 sediment production in an active rift setting. *Geology*. 47, 259-262, <https://doi.org/10.1130/G45589.1>
- 828 [73] Perissoratis, C., Piper, D.J. and Lykousis, V. 2000. Alternating marine and Lacustrine sedimentation during the
829 late quaternary in the Gulf of Corinth rift basin, central Greece. *Marine Geology*, 167, 391-411,
830 [https://doi.org/10.1016/S0025-3227\(00\)00038-4](https://doi.org/10.1016/S0025-3227(00)00038-4)
- 831 [74] Piper, D., Kontopoulos, N. and Panagos, A.G. 1988. Deltaic sedimentation and stratigraphic sequences in post-
832 orogenic basins, western Greece. *Sedimentary Geology*, 55, 283-294, [https://doi.org/10.1016/0037-](https://doi.org/10.1016/0037-0738(88)90135-2)
833 [0738\(88\)90135-2](https://doi.org/10.1016/0037-0738(88)90135-2)
- 834 [75] Poulos, S.E., Collins, M.B., Pattiaratchi, C., Cramp., A. Gull, W., Tsimplis, M. and Papatheodorou, G. 1996.
835 Oceanography and sedimentation in the semi-enclosed, deep-water Gulf of Corinth (Greece). *Marine Geology*,
836 134, 213-235, [https://doi.org/10.1016/0025-3227\(96\)00028-X](https://doi.org/10.1016/0025-3227(96)00028-X)
- 837 [76] Quack, B. and Wallace, D.W.R. 2003. Air-sea flux of bromoform: Controls, rates, and implications, *Global*
838 *Biogeochem. Cycles*, 17, 1023, <https://doi.org/10.1029/2002GB001890>
- 839 [77] Prins, M.A., Postma, G. and Weltje, G.J. 2000. Controls on terrigenous sediment supply to the Arabian Sea
840 during the Late Quaternary: the Indus fan. *Marine Geology*, 169, 351-371, [https://doi.org/10.1016/S0025-](https://doi.org/10.1016/S0025-3227(00)00086-4)
841 [3227\(00\)00086-4](https://doi.org/10.1016/S0025-3227(00)00086-4)
- 842 [78] Rohais, S., Eschard, R., Ford M., Guillocheau, F. and Moretti, I. 2007. Stratigraphic architecture of the Plio-

- 843 Pleistocene infill of the Corinth Rift: implications for its structural evolution. *Tectonophysics*, 440: 5-28,
844 <https://doi.org/10.1016/j.tecto.2006.11.006>
- 845 [79] Pemberton, S.G., Gingras, J.A.M.M.K. and Bann., K.L. 2009. Trace fossil atlas: The recognition of common
846 trace fossils in cores (short course material). pp. 1-130.
- 847 [80] Sahu, B.K. 1964. Depositional mechanisms from the size analysis of clastic sediments. *Journal of Sedimentary*
848 *Research*, 34,73-83, <https://doi.org/10.1306/74D70FCE-2B21-11D7-8648000102C1865D>
- 849 [81] Sachpazi, M., Clement, C., Laigle, M., Hirn, A. and Roussos, N. 2003. Rift structure, evolution, and
850 earthquakes in the Gulf of Corinth, from reflection seismic images. *Earth and Planetary Science Letters*, 216,
851 243-257, [https://doi.org/10.1016/S0012-821X\(03\)00503-X](https://doi.org/10.1016/S0012-821X(03)00503-X)
- 852 [82] Scholz, C.A., Johnson, T.C., Cohen, A.S., King, J.W., Peck, J.A., Overpeck, J.T., Talbot, M.R., Brown, E.T.,
853 Kalindekaf, L. and Amoako, P.Y.O. 2007. East African Megadroughts between 135 and 75 Thousand Years
854 Ago and Bearing on Early-Modern Human Origins. *Proceedings of the National Academy of Sciences of the*
855 *United States of America*, 104(42), 16416-16421, <https://doi.org/10.1073/pnas.0703874104>
- 856 [83] Sergiou, S., Beckers, A., Geraga, M., Papatheodorou, G. and Papaefthymiou, H. 2016. Recent sedimentary
857 processes in the western Gulf of Corinth, Greece: seismic and aseismic turbidites. *Bulletin of the Geological*
858 *Society of Greece*. 50, 383-391, <https://doi.org/10.12681/bgsg.11739>
- 859 [84] Shillington, D.J., McNeill, L.C., Carter, G.D.O. and the Expedition 381 Participants. 2018. Expedition 381
860 Preliminary Report: Corinth Active Rift Development. College Station, TX, International Ocean Discovery
861 Program.
- 862 [85] Shillington, D.J., McNeill, L.C., Carter, G.D.O. and the Expedition 381 Participants. 2019. International Ocean
863 Discovery Program Expedition 381 Preliminary Report. International Ocean Discovery Program; College

- 864 Station: 1-36, <https://doi.org/10.14379/iodp.pr.381.2019>
- 865 [86] Singh, R., Kumar, R., Bahuguna, I.M. and Kumar, R. 2020. Grain Size Analysis of Dune and Bar Sediments
866 of the Shyok River between Khalsar and Hunder Village, Karakoram Range, Ladakh, India. Journal of the
867 Geological Society of India, 95, 183-189, <https://doi.org/10.1007/s12594-020-1408-1>
- 868 [87] Singh, M., Singh, I.B. and Mueller, G. 2007. Sediment characteristics and transportation dynamics of the ganga
869 river. Geomorphology, 86, 144-175, <https://doi.org/10.1016/j.geomorph.2006.08.011>
- 870 [88] Sommerville, D, J.P., Mountney, N.P., Colombera, L. and Collier, R.E.LI. 2019. Impact of a pre-existing
871 transverse drainage system on active rift stratigraphy: An example from the Corinth Rift, Greece. Basin
872 Research, 32, 764-788, <https://doi.org/10.1111/bre.12396>
- 873 [89] Styzen, M.J. 1997. Cascading Counts of Nannofossil Abundance. J. Nannoplankton Res. 19.
- 874 [90] Stefatos, A., Charalambakis, M., Papatheodorou, G. and Ferentinos, G. 2006. Tsunamigenic sources in an
875 active European half-graben (Gulf of Corinth, central Greece). Marine Geology, 232, 35-47,
876 <https://doi.org/10.1016/j.margeo.2006.06.004>
- 877 [91] Sun, D.H., Bloemendal J., Rea, D.K., Vandenberghe, J., Jiang, F.C., An, Z.S. and Su, R.X. 2002. Grain-size
878 distribution function of polymodal sediments in hydraulic and aeolian environments, and numerical
879 partitioning of the sedimentary components. Sedimentary Geology, 152, 263-277,
880 [https://doi.org/10.1016/S0037-0738\(02\)00082-9](https://doi.org/10.1016/S0037-0738(02)00082-9)
- 881 [92] Taylor, B., Weiss, J.R., Goodliffe, A.M., Maria, S., Mireille, L. and Alfred, H. 2011. The structures, stratigraphy
882 and evolution of the Gulf of Corinth rift, Greece. Geophysical Journal International, 185, 1189-1219,
883 <https://doi.org/10.1111/j.1365-246X.2011.05014.x>
- 884 [93] Tyler, S.W. and Wheatcraft, S.W. 1992. Fractal Scaling of Soil Particle-Size Distributions: Analysis a

- 885 nd Limitations. Soil Science Society of America Journal, 56, 362-369, <https://doi.org/10.2136/sssaj199>
- 886 [2.03615995005600020005x](https://doi.org/10.2136/sssaj199.2.03615995005600020005x)
- 887 [94] Woodford, A.O. 1933. Origin and environments of source sediments of petroleum Paker D. Trask. The Journal
- 888 of Geology, 41, 444-445, <https://doi.org/10.2307/30058975>
- 889 [95] Udden, J.A. 1914. Mechanical composition of clastic sediments. GSA Bulletin, 25, 655-744,
- 890 <https://doi.org/10.1130/GSAB-25-655>
- 891 [96] Udden, J.A. 1898. Mechanical composition of wind deposits. Augustana Library Publications, 8, 838-839,
- 892 <https://doi.org/10.1126/science.8.206.838.b>
- 893 [97] Visher, G.S. 1969. Grain-size distributions and depositional processes. Journal of Sedimentary Research, 39,
- 894 1074-1106, <http://jsedres.sepmonline.org/cgi/doi/10.1306/74D71D9D-2B21-11D7-8648000102C1865D>
- 895 [98] Watkins, S.E., Whittaker, A.C., Bell, R.E., Brooke, S.A.S., Ganti, V., Gawthorpe, R.L., McNeill, L.C. and
- 896 Nixon, C.W. 2020. Straight from the source's mouth: Controls on field-constrained sediment export across the
- 897 entire active Corinth Rift, central Greece. Basin Research, 32, 1600- 1625, <https://doi.org/10.1111/bre.12444>
- 898 [99] Wentworth, C.K. 1922. A scale of grade and class terms of clastic sediments. The Journal of Geology, 30, 377-
- 899 392, <https://doi.org/10.1086/622910>
- 900 [100] Weltje, G.J. and Tjallingii, R. 2008. Calibration of XRF core scanners for quantitative geochemical logging of
- 901 sediment cores: theory and application. Earth and Planetary Science Letters, 274, 423-438,
- 902 <https://doi.org/10.1016/j.epsl.2008.07.054>
- 903 [101] Xiao, S.B., Li, A.C., Liu J.P., Chen, M.H., Xie, Q., Jiang, F.Q., Li, T.G., Xiang, R. and Chen, Z. 2006.
- 904 Coherence between solar activity and the East Asian winter monsoon variability in the past 8000 years from
- 905 Yangtze River-derived mud in the East China Sea. Palaeogeography Palaeoclimatology Palaeoecology, 237,

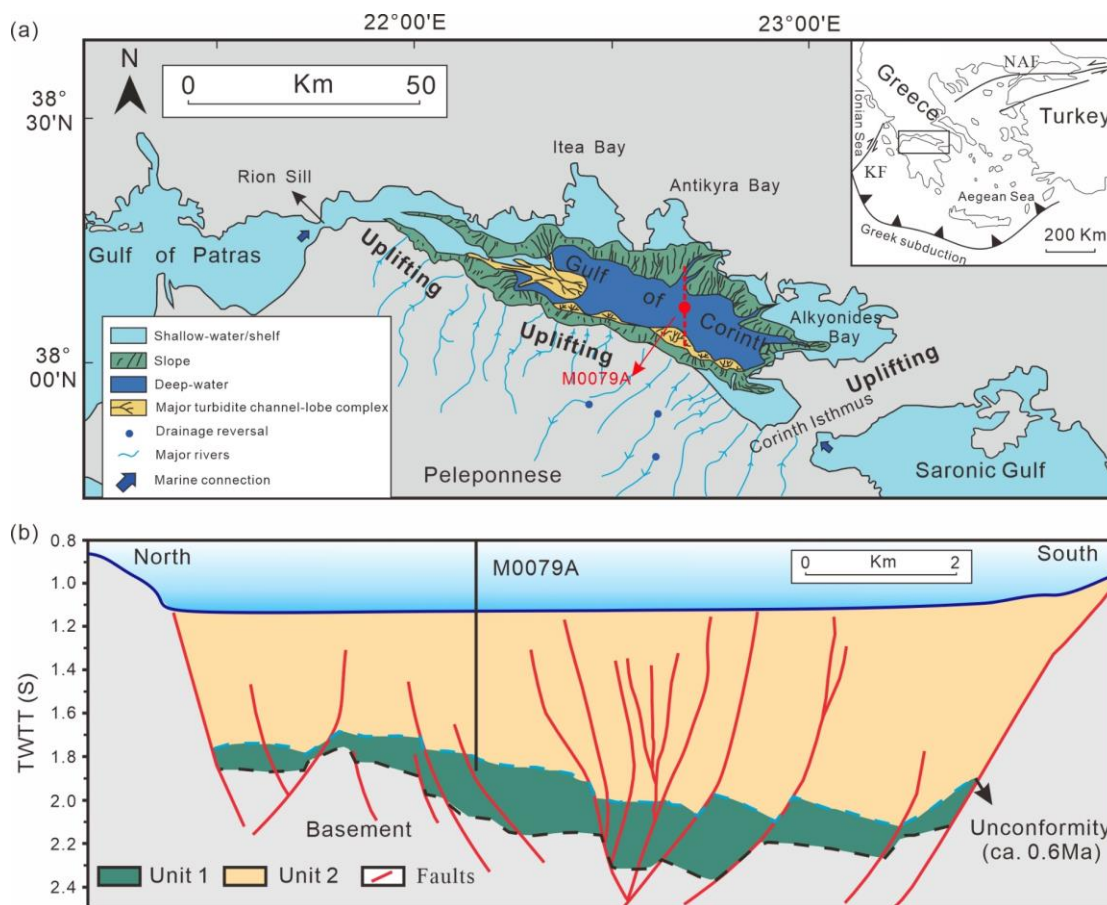
- 906 293-304, <https://doi.org/10.1016/j.palaeo.2005.12.003>
- 907 [102] Xiao, S.B. and Li, A.C. 2005. A study on environmentally sensitive grain-size population in inner shelf of the
908 East China Sea (in Chinese with English abstract). *Oceanologia et Limnologia Sinica*, 23, 27-34.
- 909 [103] Yuan, J., Yang, X.J., Lu, Z.Y., Chen, W.J., Fan, H.L. and Yuan, L.R. 2011. Probability cumulative grain-size
910 curves in sandy conglomerate of the upper Es4 in Yan22 block, Dongying depression (in Chinese with English
911 abstract). *Acta Sedimentologica Sinica*, 29, 815-524.
- 912 [104] Zhang, T.L., Wang, R.J., Xiao, W.S., Polyak, L., Astakhov, A., Dong, L.S., Wang, C.J., Liu, Y.G. and Shi, X.F.
913 2021. Characteristics of terrigenous components of Amerasian Arctic Ocean surface sediments: Implications
914 for reconstructing provenance and transport modes. *Marine Geology*, 437, 106497,
915 <https://doi.org/10.1016/j.margeo.2021.106497>
- 916 [105] Zhong, S.J. and Mucci, A. 1989. Calcite and aragonite precipitation from seawater solutions of various
917 salinities: Precipitation rates and overgrowth compositions. *Chemical Geology*, 78(3-4): 283-299,
918 [https://doi.org/10.1016/0009-2541\(89\)90064-8](https://doi.org/10.1016/0009-2541(89)90064-8)
- 919 [106] Zulhikmah, Yuskar, Y., Putra, P.S., Nugroho, S.H. and Choanji, T. 2020. Characteristics of Quaternary Deep
920 Sea Sediment in the Sumba Strait based on Grain Size and LoI (Lost on ignition Analysis). IOP Conference
921 Series: Materials Science and Engineering. 797, 012004, <https://doi.10.1088/1757-899X/797/1/012004>

922

923

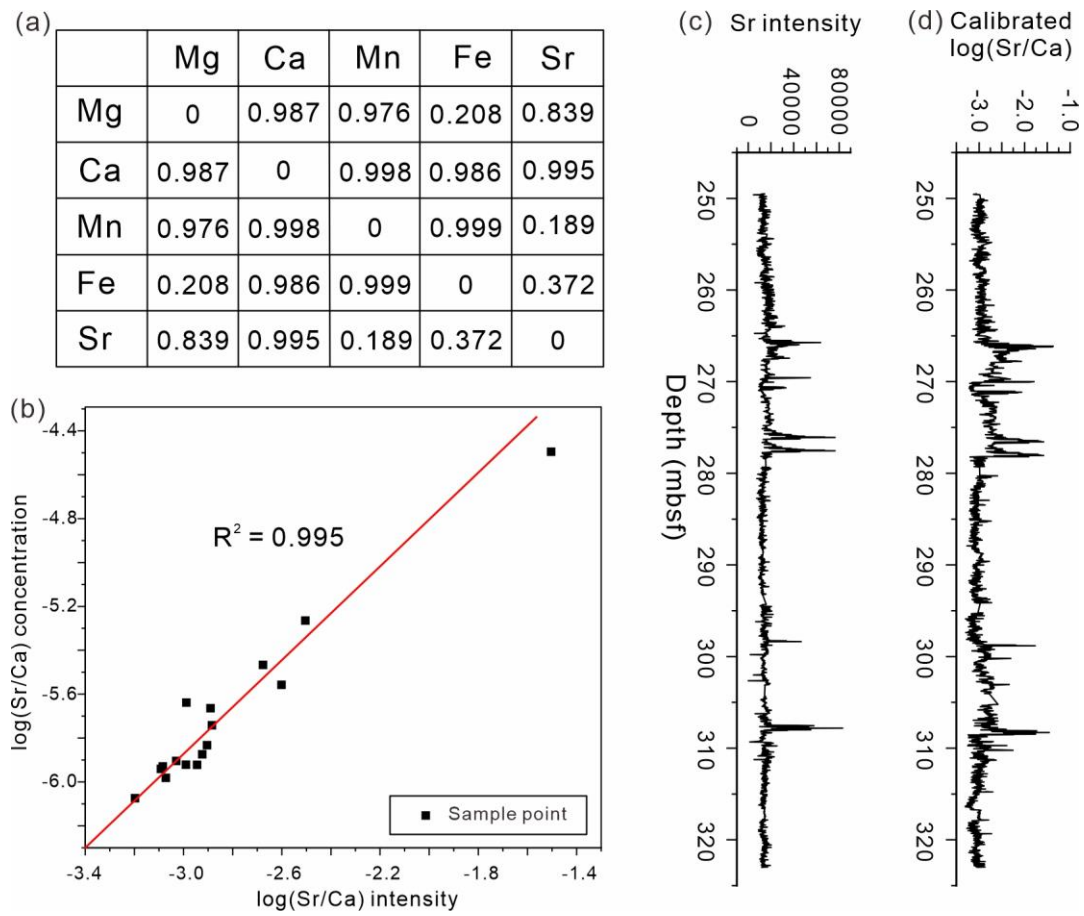
924 **Figures**

925 Fig. 1. General structure and geography of the Corinth Rift. (a) Location and tectono-sedimentologica map of the
 926 Gulf of Corinth. The red dot shows the location of site M0079A. The red dashed line shows the location of profile
 927 in b. Part of the tectono-sedimentological of the Corinth rift during the Late Pleistocene from Gawthorpe et al.
 928 (2018). Drainage reversal from Ford et al. (2016). NAF, North Anatolian Fault; KF, Kephallonia Fault. (b) Map of
 929 the N-S seismic features through site M0079A. Interpretations from Nixon et al. (2016) (faults from the authors'
 930 own mapping). Unit 1 is older, generally non-reflective and poorly stratified (Bell et al. 2009). Unit 2 is younger,
 931 stratified and cyclical (Bell et al. 2009). The estimated age of the unit 1/2 unconformity of ca. 0.6 Ma (Bell et al.,
 932 2008; Nixon et al., 2016). Inset: seismic line and drill site locations.



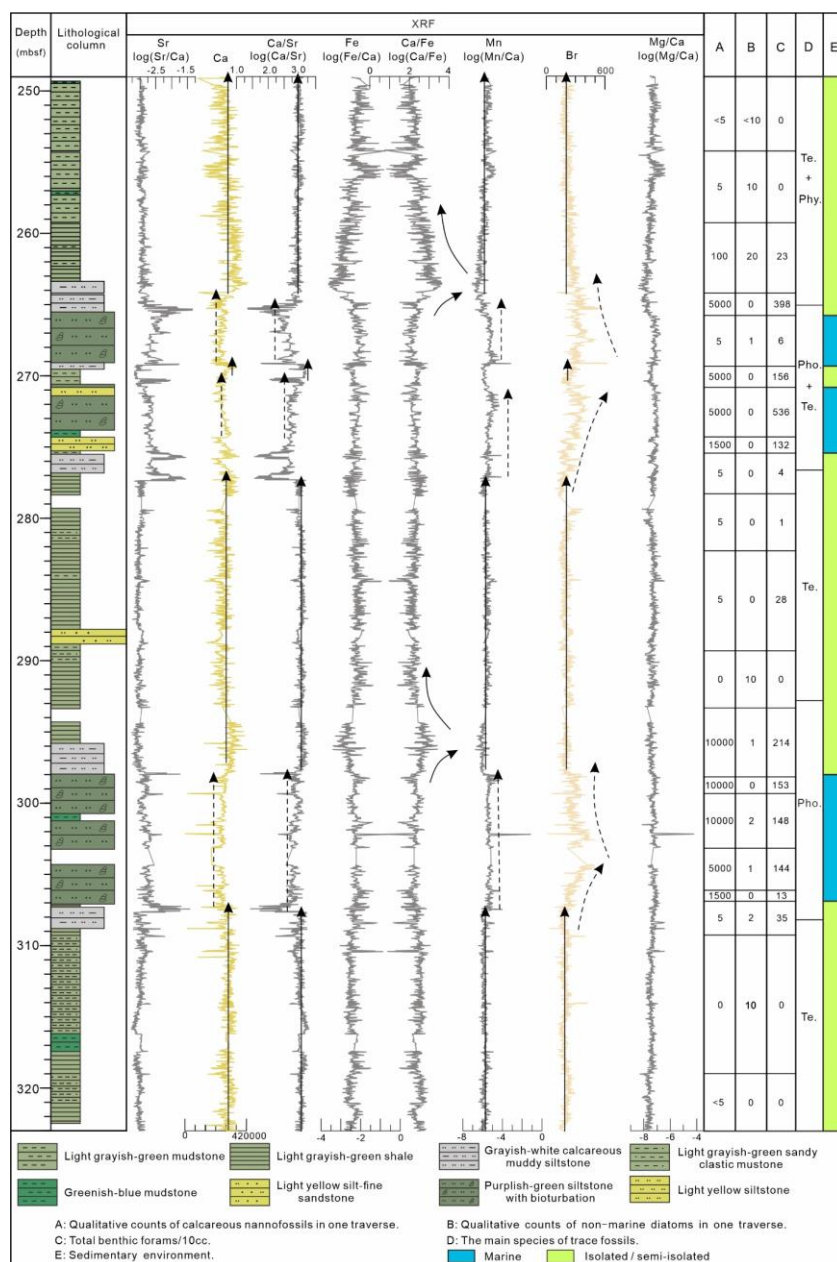
933
 934

935 Fig. 2. X-ray fluorescence (XRF) calibration workflow. (a) A log-ratio calibration (LRCE) approach (Weltje &
 936 Tjallingii, 2008) was employed to obtain optimum log-ratio denominator (in this case 'Ca'). The concentration of
 937 5 elements (Ca, Fe, Mg, Mn and Sr) was selected in 16 ground sediment samples. The Br element is not selected
 938 due to showing too low concentrations. (b) Intensity and concentration calibration of the log (Sr/Ca). (c) The
 939 detailed compositional profiles of the Sr element (expressed as intensity counts). (d) The calibrated log ratio profiles.



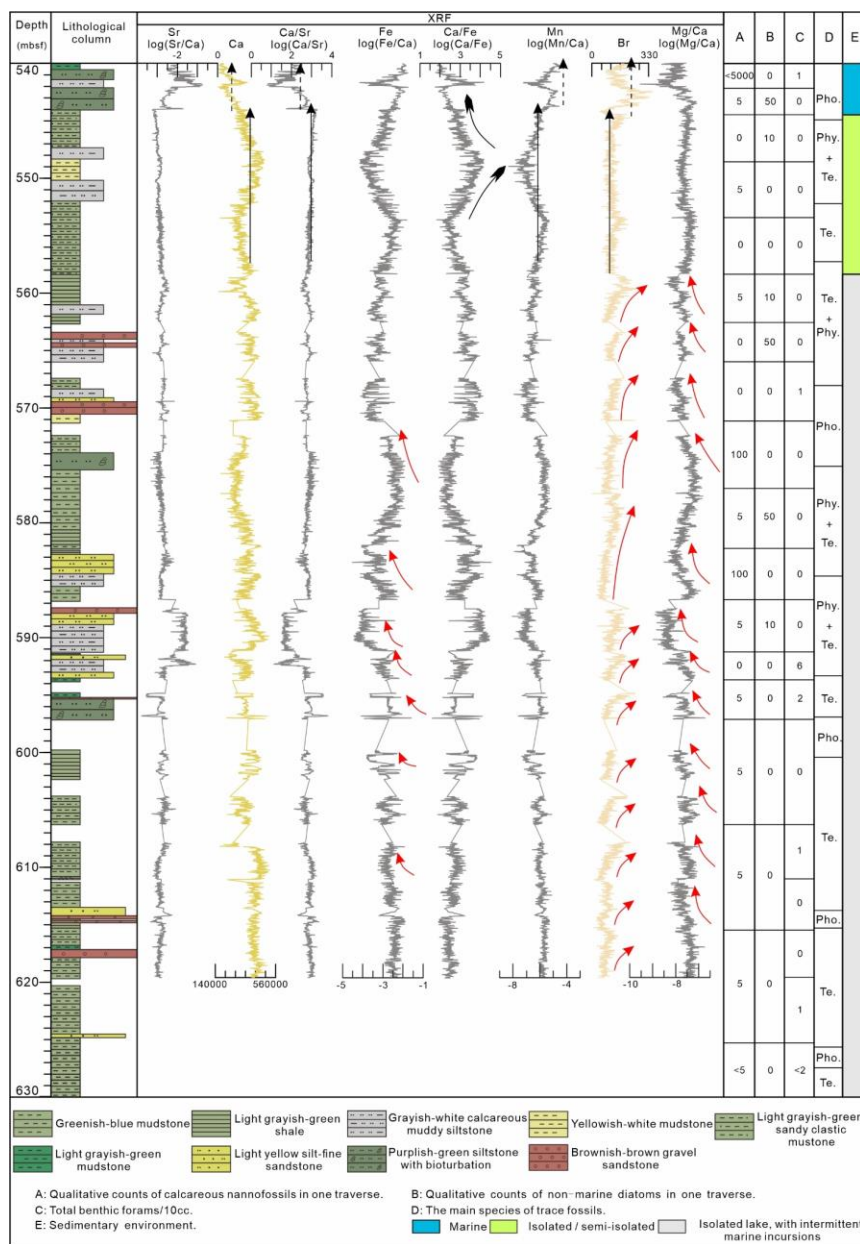
940

941 Fig. 3. The lithological column and geochemistry element curves with depth of the 249-323 mbsf intervals. Sr
 942 (strontium), Ca (calcium), Fe (iron), Mn (manganese), Br (bromine), Ca/Sr ratio, Ca/Fe ratio, and Ma/Ca ratio counts
 943 from the XRF core scanner (the curves of Br and Ca elements were expressed as intensity counts; the curves of light
 944 gray were calibrated log ration, and were expressed as dimensionless units). Black arrows and black dashed arrows
 945 indicate the curves changing trends. The data of columns A, B, and C were from McNeill et al. (2019). Column D
 946 (authors' own recognized from cores): Pho., *Phoebichnus*; Te., *Teichichnus*; Phy., *Phycosiphon*.



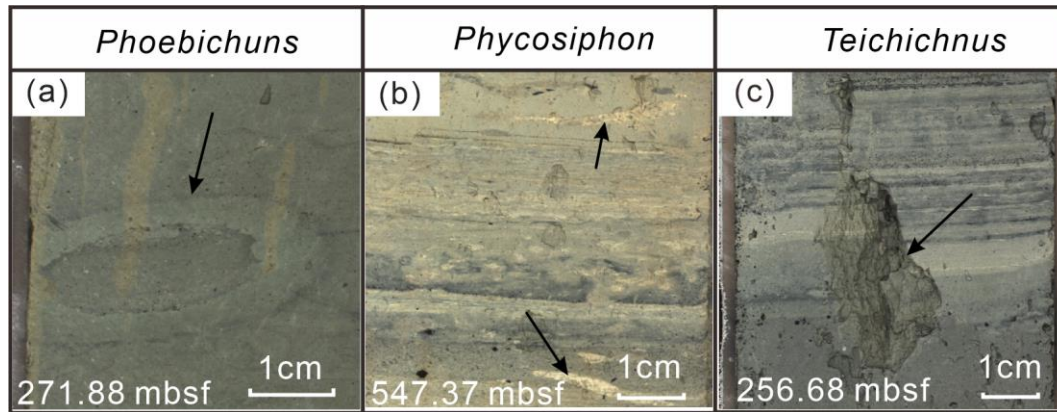
947

948 Fig. 4. The lithological column and geochemistry element curves with depth of the 540-630 mbsf intervals. Sr
 949 (strontium), Ca (calcium), Fe (iron), Mn (manganese), Br (bromine), Ca/Sr ratio, Ca/Fe ratio, and Ma/Ca ratio counts
 950 from the XRF core scanner (the curves of Br and Ca elements were expressed as intensity counts; the curves of light
 951 gray were calibrated log ration, and were expressed as dimensionless units). Black arrows, black dashed arrows and
 952 red arrows indicate the curves changing trends. The data of columns A, B, and C were from McNeill et al. (2019).
 953 Column D (authors' own recognized from cores): Pho., *Phoebichnus*; Te., *Teichichnus*; Phy., *Phycosiphon*.



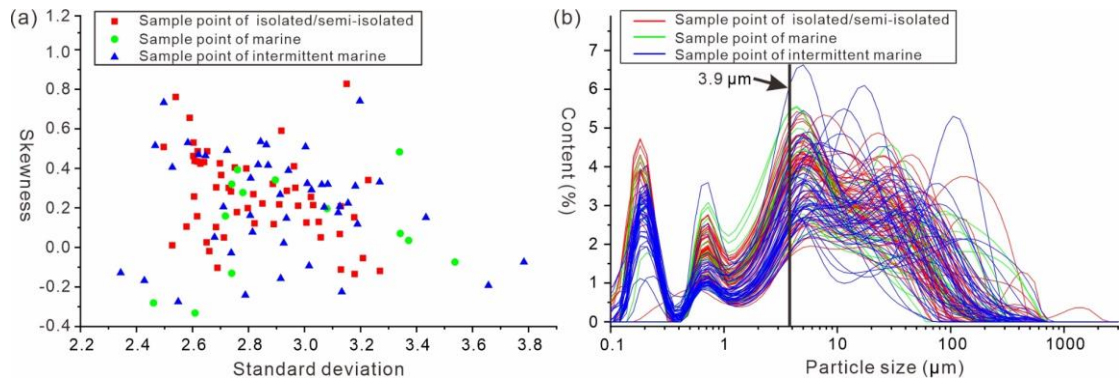
954

955 Fig. 5. Core photographs from site M0079A showing examples of trace fossils. (a) Oblique transverse cross section
956 through a radiating burrow of *Phoebichnus*. This radial burrow is approximately 1 cm in diameter. (b) In the core,
957 *Phycosiphon* appears as tiny yellow spots (transverse section) and yellow lines (longitudinal section). (c) *Teichichnus*
958 appears as a series of wavy, tightly packed, and long laminate in core sections.



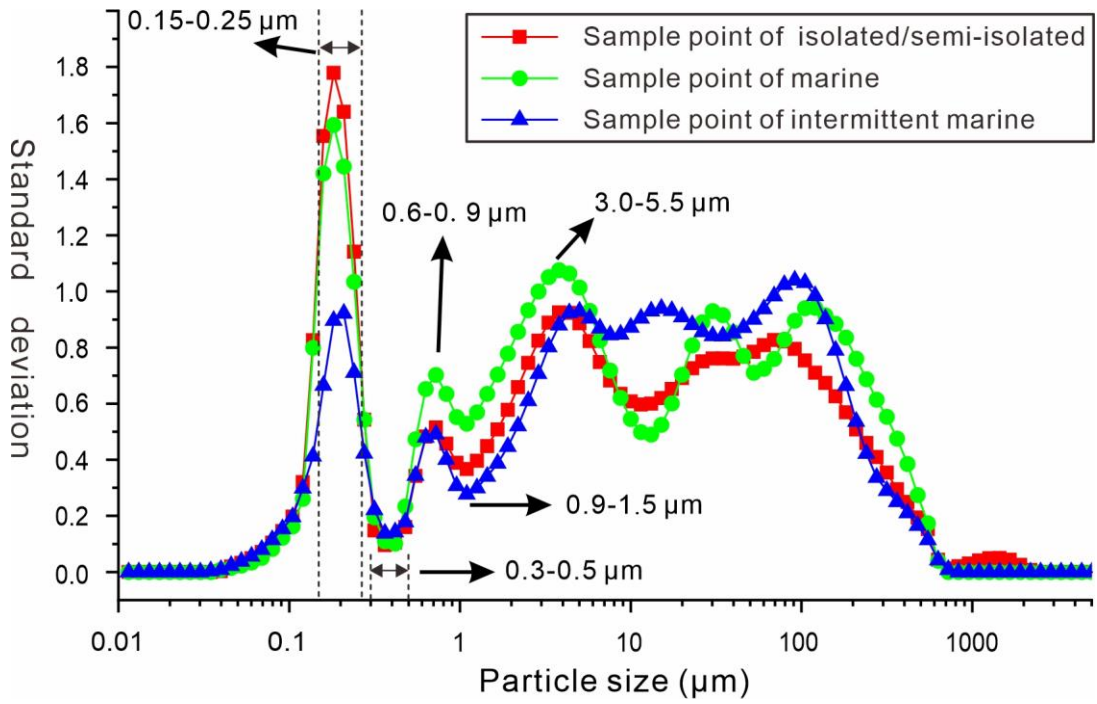
959

960 Fig. 6. Discrimination of sedimentary provenance and frequency distribution curve. (a) The skewness-standard
961 deviation diagram of core M0079A samples at study intervals; (b) Grain-size frequency distribution of core M0079A
962 samples at study intervals.



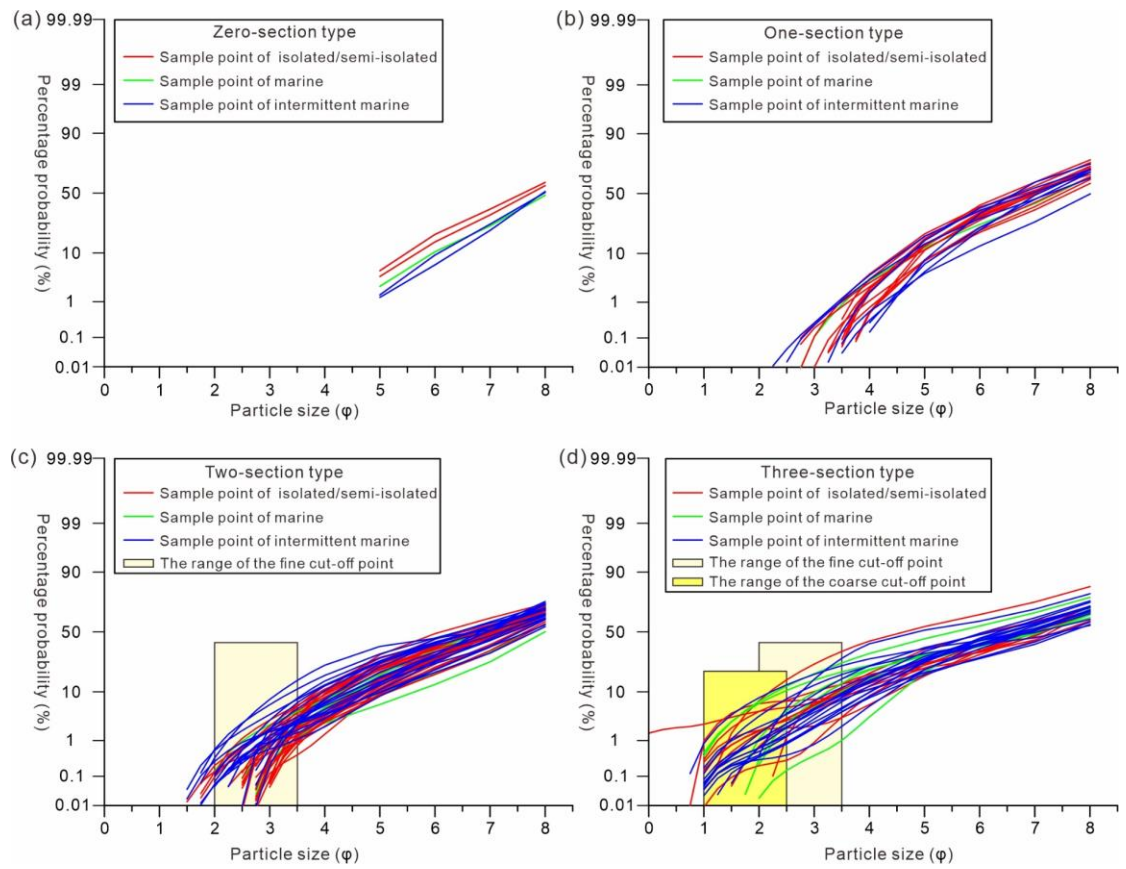
963

964 Fig. 7. Standard deviation vs. grain-size of core M0079A samples at study intervals.

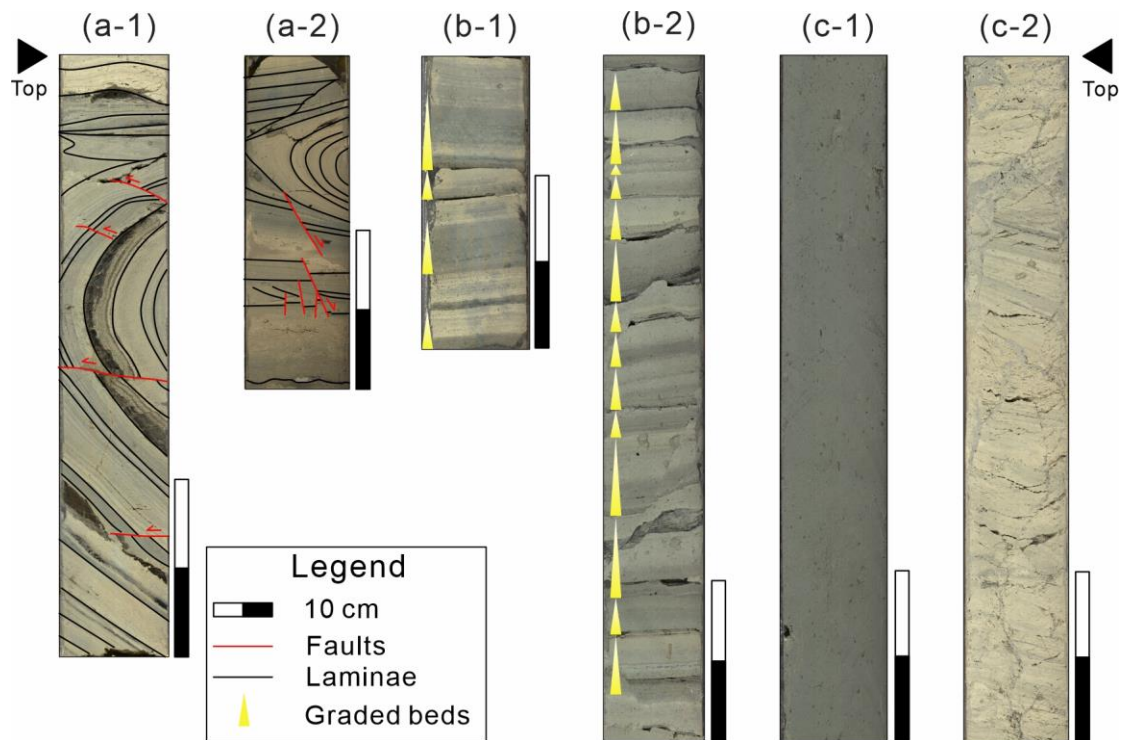


965

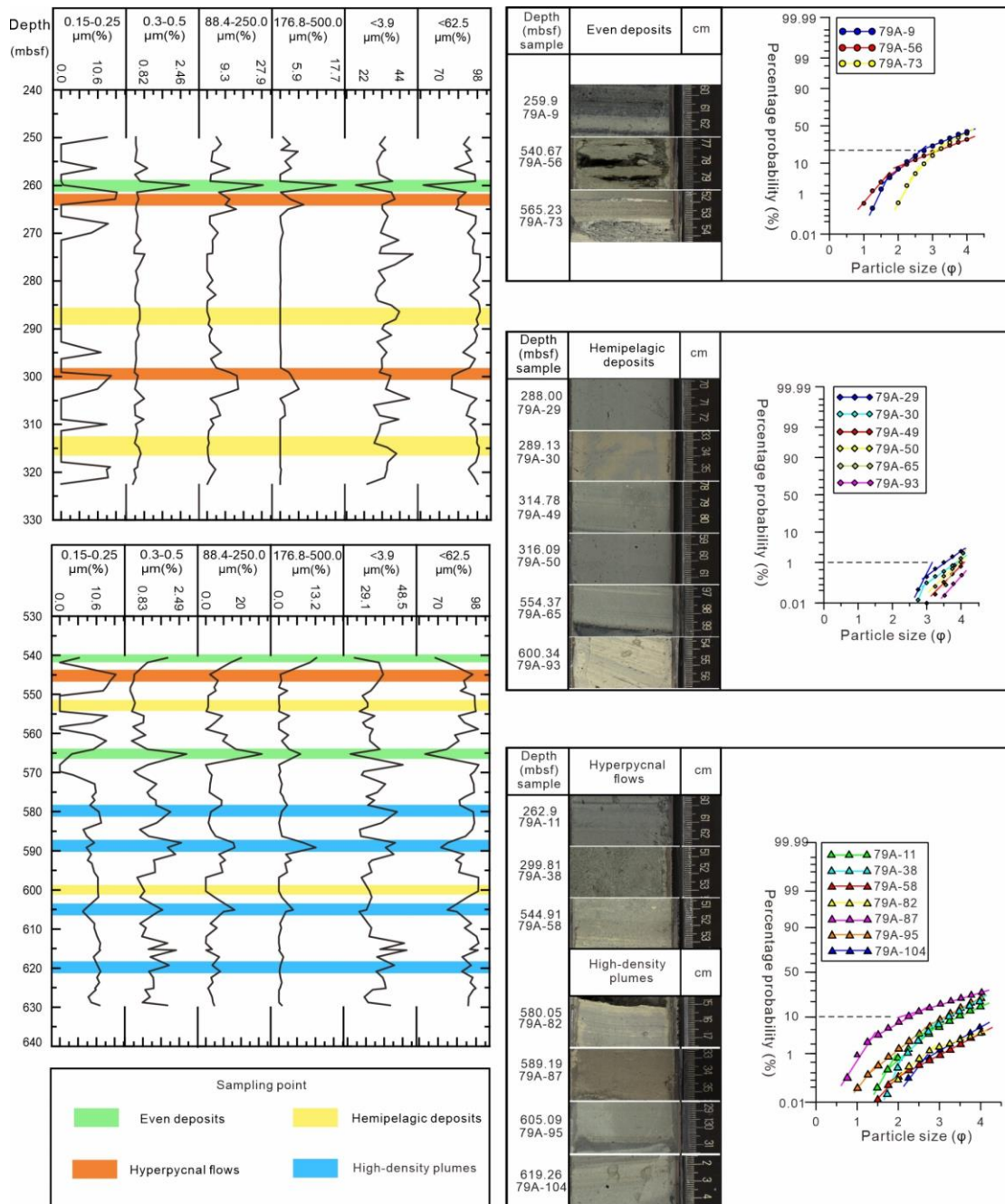
Fig. 8. The probability cumulative curves of core M0079A samples at study intervals.



968 Fig. 9. Core photographs from site M0079A showing examples of (a) example of two slumped beds (a-1: Core 129R-
 969 1, borehole depth 564.28-564.63 mbsf; a-2: Core 130R-3, borehole depth 570.33-570.54 mbsf), (b) Graded beds (b-
 970 1: Core 132R-2, borehole depth 580.04-580.21 mbsf; b-2: Core 141R-3, borehole depth 619.02-619.44 mbsf), which
 971 generated by weak and dilute flows, (3) Homogeneous muds (c-1: Core 71R-3, borehole depth 287.84-288.24 mbsf),
 972 and mud beds with continuous white laminations (c-2: Core 137R-1, borehole depth 600.21-600.61 mbsf).

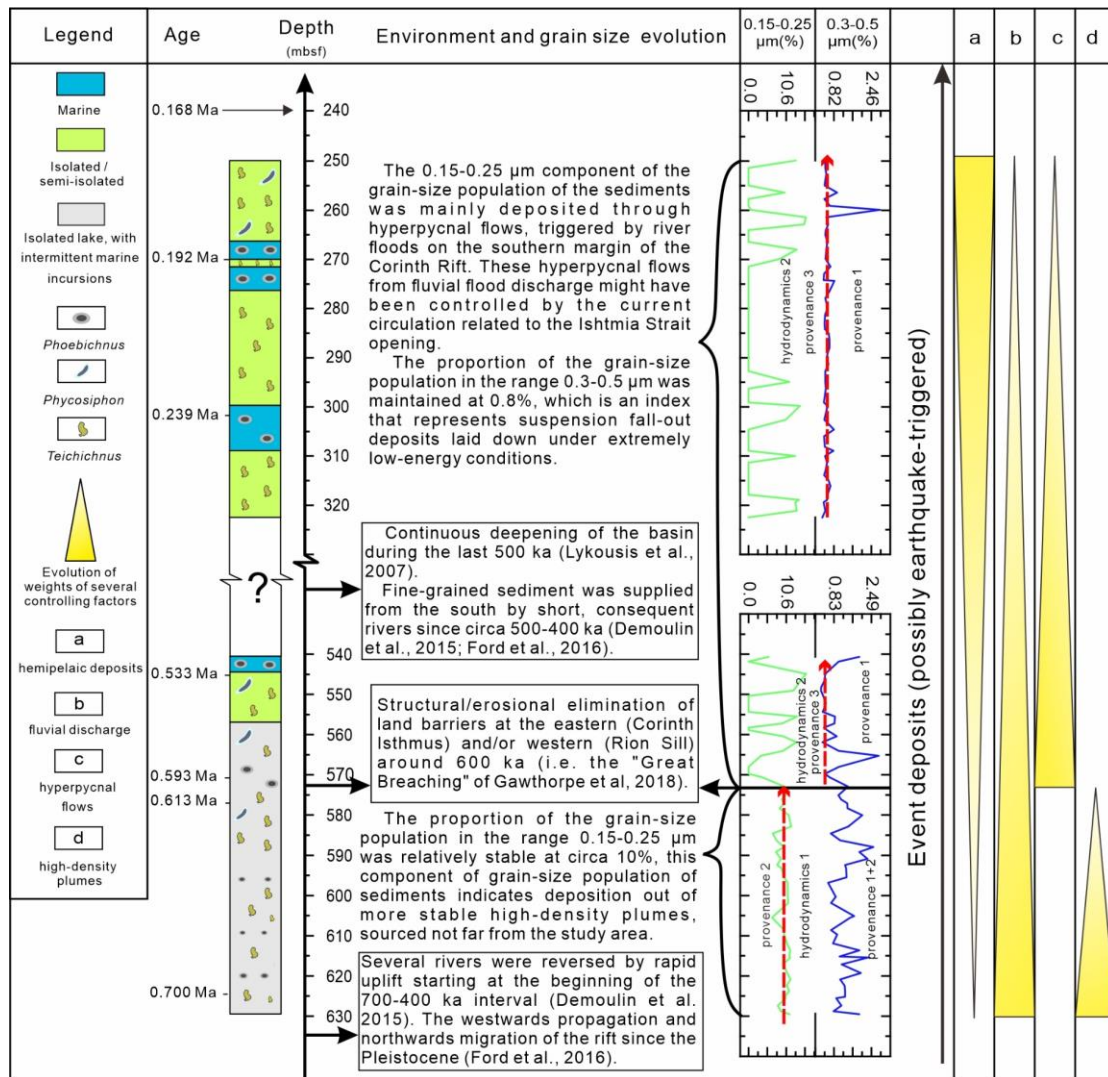


974 Fig. 10. Left: grain-size curves with depth of the study section. Right: photograph of core and probability
 975 accumulation curve of the sampling point of hole M0079A, the criterion of probability accumulation curve refers to
 976 Visher (1969).



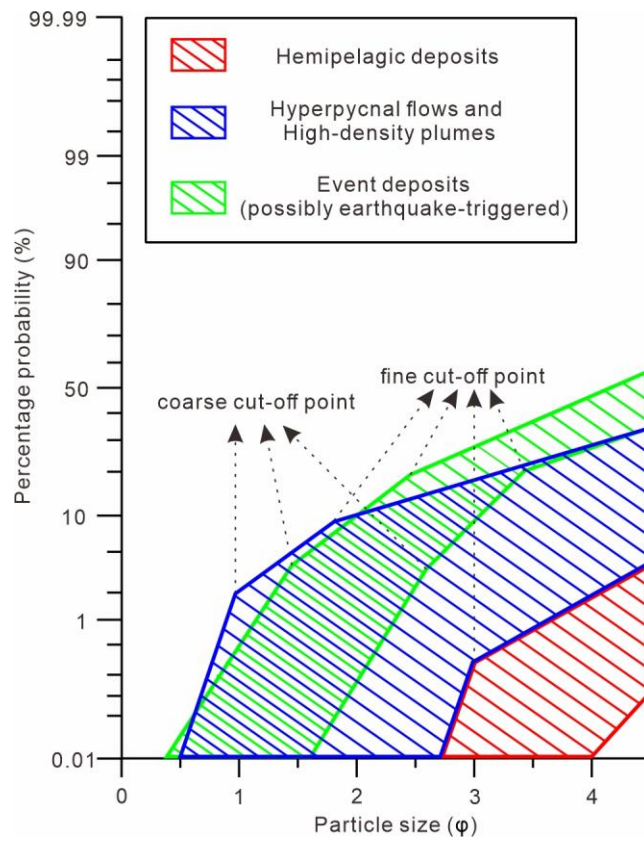
977

978 Fig. 11. Evolution of sedimentary environment, hydrodynamics, and provenance in the study area. Environment
 979 evolution from the authors' own analyses, see Figures 3 and 4. The evolution of weights of several controlling factors
 980 is used to represent the trend of change.



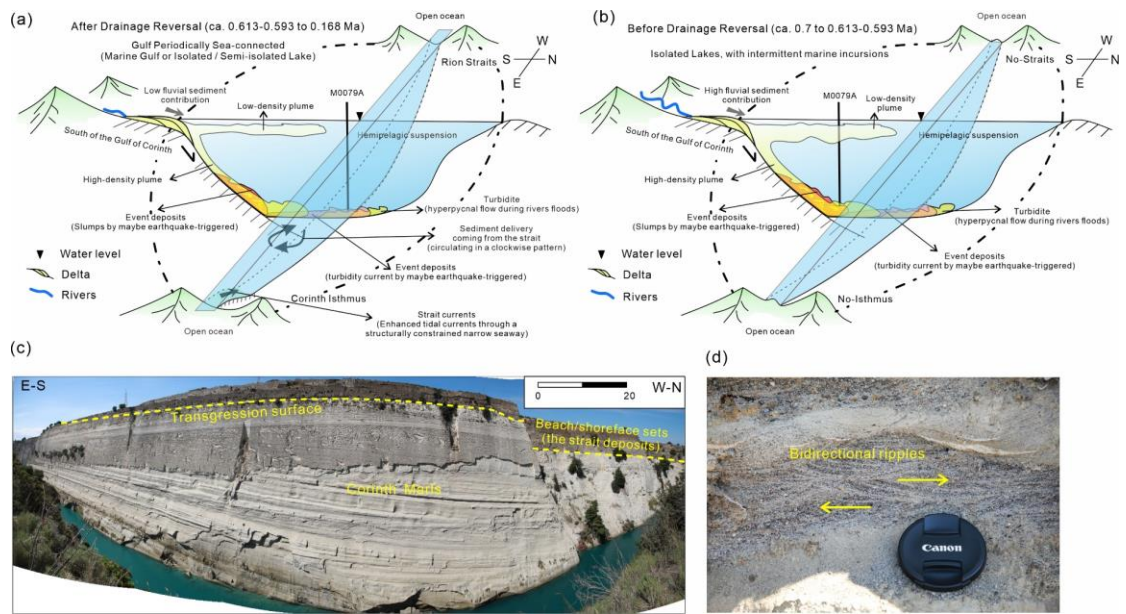
981

982 Fig. 12. Probability accumulation curve chart for distinguishing provenance and hydrodynamic in the study area.



983

984 Fig. 13. Schematic cross sections summarizing the hydrodynamic and provenance interpretations for the M0079A
 985 site for the Gulf of Corinth. (a) Gulf periodically sea-connected after drainage reversal of the south of the Gulf of
 986 Corinth. (b) Isolated lakes with intermittent marine incursions before drainage reversal of the south of the Gulf of
 987 Corinth. (c) Photomosaic of sedimentary sequences on the Corinth Isthmus. (d) The bidirectional ripples within fine
 988 sandstones. The lens cap is 6 cm in diameter.



989